SANDIA REPORT
SAND2009-5977
Unlimited Release
Printed September 2009

Compositional Ordering and Stability in Nanostructured, Bulk Thermoelectric Alloys

D.L. Medlin, J.D. Sugar, P.A. Sharma, M. Hekmaty, J. Lensch-Falk,
F. Leonard, S. Faleev

Prepared by
Sandia National Laboratories
Albuquerque, New Mexico 87185 and Livermore, California 94550

Sandia is a multiprogram laboratory operated by Sandia Corporation,
a Lockheed Martin Company, for the United States Department of Energy's
National Nuclear Security Administration under Contract DE-AC04-94AL85000.

Approved for public release; further dissemination unlimited.

Sandia National Laboratories

Issued by Sandia National Laboratories, operated for the United States Department of Energy by Sandia Corporation.

NOTICE: This report was prepared as an account of work sponsored by an agency of the United States Government. Neither the United States Government, nor any agency thereof, nor any of their employees, nor any of their contractors, subcontractors, or their employees, make any warranty, express or implied, or assume any legal liability or responsibility for the accuracy, completeness, or usefulness of any information, apparatus, product, or process disclosed, or represent that its use would not infringe privately owned rights. Reference herein to any specific commercial product, process, or service by trade name, trademark, manufacturer, or otherwise, does not necessarily constitute or imply its endorsement, recommendation, or favoring by the United States Government, any agency thereof, or any of their contractors or subcontractors. The views and opinions expressed herein do not necessarily state or reflect those of the United States Government, any agency thereof, or any of their contractors.

Printed in the United States of America. This report has been reproduced directly from the best available copy.

Available to DOE and DOE contractors from
U.S. Department of Energy
Office of Scientific and Technical Information
P.O. Box 62
Oak Ridge, TN 37831

Telephone: (865) 576-8401
Facsimile: (865) 576-5728
E-Mail: reports@adonis.osti.gov
Online ordering: http://www.osti.gov/bridge

Available to the public from
U.S. Department of Commerce
National Technical Information Service
5285 Port Royal Rd.
Springfield, VA 22161

Telephone: (800) 553-6847
Facsimile: (703) 605-6900
E-Mail: orders@ntis.fedworld.gov
Online order: http://www.ntis.gov/help/ordermethods.asp?loc=7-4-0#online

SAND2009-5977
Unlimited Release
Printed September 2009

Compositional Ordering and Stability in Nanostructured, Bulk Thermoelectric Alloys

D.L. Medlin, J.D. Sugar, P.A. Sharma, M. Hekmaty, J. Lensch-Falk,
F. Leonard, S. Faleev*
Sandia National Laboratories
P.O. Box 969
Livermore, CA. 94551-0969

*present address:
Seagate Technology
1 Waterfront Place
Pittsburgh PA 15222

Abstract

Thermoelectric materials have many applications in the conversion of thermal energy to electrical power and in solid-state cooling. One route to improving thermoelectric energy conversion efficiency in bulk material is to embed nanoscale inclusions. This report summarize key results from a recently completed LDRD project exploring the science underpinning the formation and stability of nanostructures in bulk thermoelectric and the quantitative relationships between such structures and thermoelectric properties.

ACKNOWLEDGMENTS

The authors acknowledge the helpful support in the TEM laboratory by Mark Homer and support by electron optics group including Nancy Yang, Miles Clift, Jeff Chames, and Andy Gardea. This work was performed under the Laboratory-Directed Research and Development program at Sandia National Laboratories, a multiprogram laboratory operated by Sandia Corporation, a Lockheed Martin Company, for the United States Department of Energy's National Nuclear Security Administration under contract DE-AC04-94-AL85000.

Contents

1. Introduction.....10

2. Precipitation Mechanisms in Rocksalt Structured Tellurides: $AgSbTe_2$ 12

2.1 Precipitation of Ag_2Te in $AgSbTe_2$.....12

2.1.1 Phase stability and crystal structure.....12

2.1.2 Experimental Procedure.....13

2.1.3 Results.....14

2.1.4 Origin and Significance of the Orientation Relationship.....17

2.2 Interfacial Defect Structure at Sb_2Te_3 Precipitates in $AgSbTe_2$ 26

2.2.1 Experimental Procedure.....26

2.2.2 Results and Discussion.....27

2.2.3 Conclusion.....29

3. Influence of Nanostructuring and Heterogeneous Nucleation on zT in $AgSbTe_2$.....37

3.1 Introduction.....37

3.2 Experimental Procedures.....37

3.2.1 Sample Preparation.....37

3.2.2 Microscopy and Transport Measurements.....38

3.2.3 Link Between precipitation and Transport Measurements.....38

3.3 Results.....39

3.3.1 Thermoelectric Transport and Effective Medium Behavior.....39

3.3.2 Precipitate Microstructure and Heterogeneneous Nucleation.....41

3.4 Discussion and Conclusions.....43

4. Theory of Thermoelectric Enhancement Due to Nanoinclusions.....52

4.1 Charge and Heat Transport in Bulk PbTe.....52

4.2 Electron Scattering on Band-Bending Potential of Nanoinclusions.....55

4.2.1 Band-Bending Potential.....55

4.2.2 Relaxation Time for Scattering on Nanoinclusions.....56

4.2.3 Calculation of Transport Cross Section.....58

4.3 Results and Discussion.....61

4.3.1 Enhancement of the Seebeck Coefficient and Power Factor.....61

4.3.2 Enhancement of the zT Factor.....62

4.4 Conclusion.....65

Figures

Figure 2.1 Pseudobinary Ag_2Te–Sb_2Te_3 slice of the ternary Ag–Sb–Te phase diagram. The rocksalt $AgSbTe_2$ phase is only stable in the region marked δ. Note that there exists considerable disagreement in the literature concerning the exact phase boundaries for the δ region (see text). Below 145 ◦C, the cubic β-Ag_2Te phase transforms into the monoclinic -Ag_2Te phase. Each phase is identified with a Greek letter: (a)monoclinic Ag_2Te, (b) face-centered cubic Ag_2Te, (g) body-centered cubic Ag_2Te, and (e) trigonal Sb_2Te_3. The dot-dash grey arrows identify the thermal treatment of the sample in this study.....20

Figure 2.2 Bright-field image (a) of a solidified ingot in a [0 0 1] zone axis orientation with dotted lines marking the region used for the higher-magnification dark-field images in (c)–(f). Corresponding diffraction pattern (b) with extra reflections that do not belong to a disordered rocksalt structure are labeled c, d, e, f, p, q, and r. Each image (c)–(f) corresponds to its respective extra reflection in (b). A comparison between simulated zone axis diffraction patterns for (g) three variants of the tetragonal structure (orange, blue, green, and black for reflections shared by all variants), and (h) four orientation variants of a monoclinic Ag_2Te (purple, red, blue, and green) phase in a cubic, d (black) matrix show that (h) is the more likely possibility because d, e, and f in (b) are not collinear.....21

Figure 2.3a Measured *d*-spacings from several indexed high-symmetry zone axes and corresponding diffraction patterns from matrix and precipitate phase.....23

Figure 2.3(b-d) Corresponding (b) BF and (c) DF images of secondary branches of lamellae that formed during eutectic solidification. The intensity of the EDS spectra in (d) of the blue and red points shown in (b) and (c) shows that the precipitate is enriched in Ag. The intensity ratio of AgLα/TeLα is 1.2 in the precipitate, compared to 0.72 in the matrix. Accurate compositional quantification is not possible because the precipitates are embedded in the matrix.....24

Figure 2.4 (a) Schematic showing the relationship between the cubic basis vectors $\mathbf{a_1}$, $\mathbf{a_2}$, and $\mathbf{a_3}$ and the monoclinic basis vectors **a**, **b**, and **c** of Ag_2Te. Only the Te atoms are shown. Small displacements of the Te atoms relative to the ideal cubic structure shown in (a) occur rapidly during the diffusionless transformation at 145◦C and result in the observed monoclinic structure. The monoclinic unit cell is shown in red. Three other symmetric variants, which are shown in (b), (c), and (d), are related to (a) by a 90◦rotation about $\mathbf{a_3}$, a 90◦ rotation about $\mathbf{a_2}$, and a 90◦ rotation about $\mathbf{a_2}$ followed by a 90◦ rotation about $\mathbf{a_3}$, respectively. There are a total of 12 symmetric variants of the orientation relationship.....25

Figure 2.5. Schematic showing crystal structures for the (a) rock-salt and (b) tetradymite structured tellurides. The rocksalt structure (a) is projected along $[10\bar{1}]$ and the tetradymite structure (b) is projected along $[\bar{2}110]$. For both phases the stacking of the close-packed planes are given by the lettering with the metal (e.g. Ag, Sb) and tellurium planes indicated by Greek and Roman letters, respectively.....33

Figure 2.6. (a) TEM micrograph showing example of an Sb_2Te_3 plate in rock-salt $AgSbTe_2$ matrix. Electron diffraction (b) shows that these plates are oriented with $(0001)_{Sb_2Te_3} \parallel (111)_{AgSbTe_2}$ and $[\bar{2}110]_{Sb_2Te_3} \parallel [10\bar{1}]_{AgSbTe_2}$.....34

Figure 2.7. HRTEM image and circuit analysis of the step-defect, or "disconnection," at the $AgSbTe_2/Sb_2Te_3$ interface.....35

Figure 2.8. (a)Schematic of the observed interfacial disconnection. (b) Sequence of rearrangements produced by motion of the perpendicular and parallel components of the defect.....36

Figure 3.1 Synthesis and control of nanoprecipitates in thermoelectric alloy (Ag,Sb)Te. (a) The homogeneous $AgSbTe_2$ δ phase occurs in the Ag_2Te-Sb_2Te_3 pseudobinary system. Inset: Enlarged view of phase diagram in (a). A solid state precipitation reaction δ-->δ'+$(Sb,Ag)_2Te_3$ occurs at 500 °C, where the δ phase (30 at.% Sb) decomposes into an Sb deficient (~29 at. %) d' phase with Ag-doped Sb_2Te_3 precipitates.....45

Figure 3.2 Representative transport properties of the homogeneous d (a) Seebeck coefficient (*S*) versus temperature (*T*). All samples were p-type. (b) Resistivity (ρ) versus *T*. Inset: Thermal conductivity (κ) versus *T*. (c) Hall number (R_H) versus T. Inset: The Hall resistivity (ρ_{Hall}) was linear as a function of magnetic field (*H*). All samples were p-type, in agreement with *S*(*T*), in the entire *T*-regime studied.....46

Figure 3.3 Change in average transport properties of homogeneous δ with the introduction of $(Sb,Ag)_2Te_3$ precipitates.....47

Figure 3.4 Δ*S* shares a common time dependence with the formation of Sb_2Te_3 precipitates as determined from powder X-ray diffraction. (a) Peak intensity of the [1 0 10] Sb_2Te_3 peak as a function of annealing time at 500 °C. Inset: Raw Xray intensity versus 2Q of the peak displayed in (a) at different annealing times. (b) D*S* versus annealing time shares the same time dependence as the Xray data in (a). The shaded region corresponds to the expected difference in *S* between δ and p-type Ag-doped Sb_2Te_3. *S* for (Ag,Sb)Te with $(Sb,Ag,)_2Te_3$ precipitates is bounded by that for pure (Ag,Sb)Te and pure $(Sb,Ag)_2Te_3$.....48

Figure 3.5 Transport properties compared with calculations from effective medium theory.....49

Figure 3.6 Representative microstructures observed by TEM as a function of time. Insets show electron diffraction patterns. (a) Initial microstructure of the "homogeneous" δ-phase contains large number of planar defects. (b), (c) initial precipitation occurs with metastable formation of tetradymite-type structure. (d) at long times, the equilibrium Sb_2Te_3 plates form.....50

Figure 3.7 Precipitates form a percolating network (a) Composite BF TEM image showing many planar defects. Since planar defects form an interconnected network in the unannealed δ phase. Precipitates preferentially nucleate at planar defects upon annealing. (b) Optical bright field micrograph of sample annealed for 4 hours at 500 °C. Large mm size precipitates decorate grain boundaries. Grain boundaries are therefore also nucleation sites for Sb_2Te_3 precipitates in $AgSbTe_2$.....51

Figure 4.1 (a) Schematic of the semiconductor host with metallic nanoinclusions. Panel (b) shows an example of the calculated potential $V(r)$ and the energy diagram for PbTe at T =300 K, n=2.5X10^{19} cm^{-3}, V_B=−0.11 eV, and R=1.5 nm. Panel (c) illustrates the concept of energy filtering: low energy electrons scatter strongly with the potential, but high energy electrons are unaffected. The calculated electronic relaxation time for the potential of panel (b) is also shown.....67

Figure 4.2 Calculated Seebeck coefficient for PbTe with metallic nanoinclusions as a function of the doping for several different values of the nanoinclusion radius.....68

Figure 4.3 Panel (a) shows the calculated Seebeck coefficient and conductivity for PbTe as a function of the interface potential V_B. Panel (b) shows the resulting power factor. Parameters are R=1.5 nm, T=300 K, x=5%, and n=2.5X10^{19} cm^{-3}.....69

Figure 4.4 Thermoelectric coefficients as a function of temperature calculated for n=2.5X10^{19} cm−3, x=5%, and R=1.5 nm. (a) The optimized zT factor, with the optimal values of V_B, is shown in the inset. (b) The Seebeck coefficient. (c) The electrical conductivity. Inset shows optimized (filled circles) and bulk PbTe (solid line) power factor $S^2\sigma$. (d) The thermal conductivity. In all panels, solid circles include electron and phonon scattering on the inclusions; open circles include electron scattering onthe inclusions but with bulk PbTe values of k_{ph}; solid lines and filled squares are the calculated and measured values for bulk PbTe.....70

Figure 4.5 Calculated ZT factor for PbTe illustrating the relative effects of electronic and phonon scattering on nanoinclusions. In both panels R=1.5 nm, x=5%, and T=300 K. (a) High doping n=5X10^{19} cm^{-3}. (b) Low doping n=5X10^{18} cm^{-3}. Dotted lines are calculated using the bulk phonon thermal conductivity. Filled circles correspond to the bulk PbTe system. Stars include only the phonon scattering on nanoinclusions.....71

Figure 4.6 Temperature dependence of the optimized *ZT* factor for PbTe. (a) low doping n=5X10^{18} cm^{-3} and (b) high doping n=5X10^{19} cm^{-3}. In both panels filled circles denote the optimized *zT* calculated with both electron and phonon scattering on nanoinclusions, open circles denote *zT* calculated with electron scattering on nanoinclusions and with bulk PbTe values of k_{ph}, and the solid line is for bulk PbTe. The inset in (a) shows the values of V_B that maximize *zT*. In (b) the bottom inset shows the optimal values of V_B that maximize *zT* (filled circles) and V_B^{Pb} for Pb nanoinclusions. The top inset shows the calculated power factor.....72

Tables

Table 2.1. Summary of the geometrical properties of the observed disconnection at the $AgSbTe_2/Sb_2Te_3$ interface.....31

Table 2.2. Summary of the mass flux required for motion of the disconnection at the $AgSbTe_2/Sb_2Te_3$ interface.....32

Table 4.1 Parameters used to calculate the relaxation times for bulk PbTe at *T*=300 K.....66

1. Introduction

Thermoelectric materials have many applications in the conversion of thermal energy to electrical power and in solid-state cooling [1]. The central materials research challenge is to improve the intrinsic energy conversion efficiency of the thermoelectric material. In general, materials development schemes to improve this efficiency are driven by the need to maximize the Seebeck coefficient, α (i.e. the ratio of the developed voltage and temperature difference between the points at which the voltage is measured), and to balance the competing requirements of high electrical conductivity, σ, and low thermal conductivity, κ. A useful parameter that characterizes the energy conversion efficiency of a material is the so-called thermoelectric figure-of-merit, $zT = \alpha^2 \sigma T/\kappa$. Advances over the past decade show that it is possible to enhance zT in nanoscale systems by taking advantage of quantum confinement and carrier scattering effects to enhance the power factor, $\alpha^2\sigma$, and phonon scattering at interfaces to reduce the lattice contribution to κ. Because many existing and envisioned thermoelectric applications will require a material that is itself of macroscopic dimension, recent reports of property enhancement in bulk alloys possessing nanometer-scale compositional modulations have generated much excitement [2-4]. However, to make progress on developing and applying such nanostructured, bulk thermoelectric alloys will require a greatly improved fundamental understanding of how the alloys form and the mechanisms by which the thermoelectric properties are enhanced. These issues motivate the questions posed under this LDRD project: namely, (1) *What controls the formation and thermal stability of property-enhancing nanostructures in bulk thermoelectric alloys?* and (2) *How does the nanostructure relate quantitatively to the measured thermoelectric properties?*

Under this project we chose to focus on telluride compounds based on the rocksalt and tetradymite structures. Such materials have good thermoelectric properties and are widely used in a variety of thermoelectric devices. Important examples of these materials include PbTe [5] and $AgSbTe_2$ [6], which have the rocksalt structure, and Bi_2Te_3 and Sb_2Te_3 [7], which fall within the broad tetradymite-class of structures [8]. One emerging approach to producing nanostructured thermoelectric materials is through the control of solid-state phase transformations, such as precipitation[9]. Therefore, a key element of our work was to investigate the phase transformation mechanisms in relevant nanostructured tellurides. We focused in particular on second phase formation in the rock-salt structured telluride $AgSbTe_2$, which is an important thermoelectric material in its own right as well as being a key constituent of both the TAGS and LAST class of high performance thermoelectric alloys. This work is described in section 2. Ultimately we seek to understand the quantitative relationships between the internal nanostructure and the thermoelectric performance. Our experimental work relating the formation of second-phase precipitates to thermoelectric performance in the $AgSbTe_2$ system is discussed in Section 3. Finally, our theoretical work establishing the mechanisms by which embedded nanoscale inclusions can enhance zT, through a combination of energy filtering and reduced thermal conductivity, is presented in Section 4.

2. Precipitation Mechanisms in Rocksalt-Structured Tellurides: $AgSbTe_2$

Rocksalt structured tellurides form an important class of thermoelectric materials. We chose to study several aspects second phase formation in such materials as a possible route to nanostructure. In this section we focus on second phase formation in $AgSbTe_2$. This compound is a good thermoelectric material [6, 10] and is also a critical constituent of two classes of high-performance thermoelectric material—$(AgSbTe_2)_{1-x}(GeTe)_x$ (also called TAGS) [11]and $(AgSbTe_2)_{1-x}(PbTe)_x$ (also called LAST) [2]. Both the TAGS and LAST materials have complex microstructures that are thought to enhance the thermoelectric performance by affecting the electron (increasing the Seebeck coefficient) and phonon (lowering the thermal conductivity) scattering at embedded interfaces [2] [11]. However, the factors that control the microstructural evolution in these systems and the detailed mechanisms by which nanostructural features enhance the thermoelectric performance are still poorly understood. Due to its relatively simple composition, $AgSbTe_2$ provides a good starting point for understanding the microstructure–property relationships in the more complex TAGS and LAST systems.

In Section 2.1, we discuss our study of the formation of second phase silver telluride precipitates in material of the exact $AgSbTe_2$ stoichiometry [12]. This work has helped resolve confusion in the thermoelectrics literature concerning phase-equilibria in the Ag-Sb-Te ternary system and the structure of the $AgSbTe_2$ phase. As we show, the formation of crystallographically aligned monoclinic Ag_2Te, which is consistent with some assessments of the phase diagram, produces additional diffraction peaks that can be easily misinterpreted as superlattice reflections. Our analysis of the orientation relationship sheds light on the Ag_2Te precipitation mechanisms.

In Section 2.2, we discuss our work studying the formation of tetradymite-structured Sb_2Te_3 plates in $AgSbTe_2$. Our work investigating the atomic-scale interfacial structure at such plates has provided elucidated the role that interfacial line defects can play in controlling the precipitation. This mechanism should also be generally applicable to other rocksalt/tetradymite telluride systems. Our detailed work on the $AgSbTe_2/Sb_2Te_3$ system also sets the stage for our work discussed in Section 3 on the relationship between thermoelectric transport properties and growth of second phase precipitates in this system.

2.1 Precipitation of Ag_2Te in $AgSbTe_2$

2.1.1 Phase stability and crystal structure

The equilibrium phase diagram [13] for the pseudobinary Ag_2Te–Sb_2Te_3 slice of the ternary Ag–Sb–Te system is shown in Fig. 2.1. For simplicity, the compound with approximate composition $AgSbTe_2$ is labeled as the δ phase throughout this report, since this single-phase compound exists over a wide range of stoichiometries. The single-phase compound is generally thought to be a rocksalt-structured compound with Ag and Sb atoms distributed randomly on one fcc lattice and Te on another fcc lattice displaced by

[1/2 1/2 1/2]a (a = 6.078 Å) [14]. However, recent work [15], based on X-ray diffraction, has suggested alternative ordered tetragonal and trigonal structures, reopening questions about the actual structure of $AgSbTe_2$.

There is also some disagreement in the literature about the location of the δ phase boundaries. Some assessments show the exact $AgSbTe_2$ stoichiometry as being within the δ phase boundaries over a range of temperatures [16-18], while others indicate that this stoichiometry is always in a two-phase region [13, 19]. Fig. 1 is based on this latter interpretation of the phase equilibria. Here, the single-phase δ region is enriched in Sb away from the exact composition of $AgSbTe_2$ and extends up to 31 at. % Sb at 575 °C; thus, at the exact composition of $AgSbTe_2$, and at temperatures between 360 °C and 548 °C, the system falls in the two-phase coexistence region for Ag_2Te and δ. This interpretation is supported by previous X-ray diffraction studies of $AgSbTe_2$ that have detected peaks associated with Ag_2Te (e.g., [17] [19, 20]). Although X-ray diffraction has shown the presence of Ag_2Te, there has been no detailed microstructural analysis of the system. Thus, very little is known about the formation of Ag_2Te in $AgSbTe_2$, whether as a result of the eutectic solidification process or by solid-state precipitation. The analysis is further complicated by the transformation of Ag_2Te from a cubic to a monoclinic phase when cooled below 145 °C [21, 22].

To address these compositional and structural questions, an ingot of stoichiometric $AgSbTe_2$ was prepared and its microstructure was investigated using a suite of characterization techniques. The formation of a two-phase mixture of cubic δ and monoclinic Ag_2Te was verified and the ambiguity in interpreting the δ-phase diffraction pattern was resolved. A particular focus was placed on (1) confirming that δ has the rocksalt structure, and (2) providing an explanation for the orientation relationship observed in the electron diffraction patterns between the monoclinic Ag2Te phase and δ. The analysis suggests that this relationship is a direct result of the close alignment of the Te sublattices in both the matrix and precipitate phases and likely initiates with the nucleation of high-temperature cubic Ag_2Te.

2.1.2 Experimental Procedure

A polycrystalline ingot of the stoichiometric composition, $AgSbTe_2$, was prepared by melting the elemental components and solidifying the material. The elemental components, in pellet form (99.999% pure Ag, 99.9999% pure Sb and Te, Alfa Aesar), were loaded into a quartz ampoule. This ampoule was then evacuated to a pressure less than 10^{-4} Torr and sealed. Precise measurements of the weight of the initial components determined the composition of the mixture to be 25.00 at. % Ag, 25.01 at. % Sb, and 49.99 at. % Te. The sealed quartz ampoule containing the pure elements was heated in a vertical tube furnace (Lindberg-Blue) to 800 °C and held for 8 h to produce a well-mixed liquid. The furnace was cooled at a rate of 6.67 °C/min to 600 °C and was held for 30 min just above the liquidus temperature (575 °C) before cooling at 0.1 °C/min to 500 °C. The system was held for 48 h to allow formation of the equilibrium phases and large grains. Finally, the furnace was turned off and the system was allowed to cool to 150 °C at ≈3°/min and from 150 °C to room temperature at ≈0.7°/min.

The microstructure and local composition of the ingot were analyzed using electron microprobe and transmission electron microscopy (TEM). Specimens for TEM analysis were prepared by mechanical dimpling (Gatan 656 Dimple Grinder) and argon ion milling using a liquid nitrogen cooled stage (Gatan 600 Dual Ion Mill). Coarse-scale compositional measurements were made by wavelength dispersive X-ray spectroscopy (WDS) in a microprobe (JEOL JXA-8200). Higher resolution imaging and diffraction analyses were performed using transmission electron microscopy (120 kV JEOL 1200EX and 200 kV JEOL 2010F). Compositional measurements in TEM were made by energy dispersive X-ray spectroscopy (EDS) (Oxford, Inc.).

2.1.3 Results

The combination of electron imaging, diffraction, and chemical analysis presented in the next three sections confirms that stoichiometric $AgSbTe_2$ phase separates into a mixture of monoclinic Ag_2Te and rocksalt δ with a disordered cation sublattice. First, a measured electron diffraction pattern from fine-scale microstructural features with two possible interpretations is presented. Single-phase and two-phase interpretations of the diffraction pattern are compared with the data, and evidence is presented that suggests this pattern is a result of a two-phase mixture. Larger-scale features from the same sample are isolated and electron diffraction patterns and EDS spectra from the matrix and precipitate phases are analyzed independently. The structural similarity between the large-scale and fine-scale features suggests that they are both the result of a two-phase mixture. The ambiguity in the diffraction analysis is a direct result of the crystallographic alignment of the matrix and precipitate phases, the origin of which is discussed.

Matrix/precipitate orientation relationship

A typical TEM bright-field (BF) image and diffraction pattern of the solidified ingot oriented along a [0 0 1] zone axis orientation are shown in Fig. 2.2(a) and (b). A number of reflections are present in addition to those expected for a rocksalt structure. Careful examination of the less intense “extra” reflections, such as those labeled c–f and p–r, using dark-field (DF) imaging revealed that each reflection excited a series of particles approximately 10 nm in diameter. Fig. 2.2(c)–(f) are DF images that were recorded using the reflections labeled c–f, respectively, in Fig. 2.2(b). Each “extra” reflection excites a unique and spatially distinct set of equiaxed particles.

Two possible interpretations of the diffraction are considered next. One possibility is that the material is single phase and consists of the recently proposed tetragonal structure of $AgSbTe_2$ [15]. The proposed tetragonal structure is similar to the rocksalt structure but has an ordered cation sublattice. An alternative possibility is that the material consists of two phases: monoclinic Ag_2Te precipitates in a rocksalt δ-phase matrix. This latter interpretation is consistent with the expectation from the phase diagram shown in Fig. 2.1. Specifically, at 500 °C, the equilibrium phases present in this system should be cubic Ag_2Te, which transforms to a monoclinic structure below 145 °C, and

rocksalt δ. As discussed next, diffraction simulations are consistent with the latter interpretation.

A simulated diffraction pattern of the tetragonal structure provided by Quarez et al. [15]is shown in Fig. 2.2(g). In order to replicate all of the less intense reflections of Fig. 2.2(b), it is necessary to simulate three variants of the ordered tetragonal structure that are crystallographically aligned with a specific orientation relationship. The orientation relationship is defined in the equation below:

$$\begin{aligned} &[001](110)_1 \,||\, [110](1\bar{1}0)_2 \\ &[001](110)_1 \,||\, [110](001)_3 \end{aligned} \tag{2.1}$$

where $[u\ v\ w]_i \,||\, [u\ v\ w]_j$ refers to a specific set of parallel directions, and $(h\ k\ l)_i||(h\ k\ l)_j$ refers to a specific set parallel planes in the i and j variants, respectively. In the simulation, variants 1, 2, and 3, are shown in orange, blue, and green, respectively. The black reflections are shared by all variants. The diffraction pattern variants are more easily differentiated in the less intense reflections because the more intense reflections have overlapping information.

Alternatively, the diffraction pattern in Fig. 2.2(b) can be indexed as a two-phase mixture of monoclinic Ag_2Te precipitates (a = 8.1616 Å, b = 4.46651 Å, c = 8.97335 Å, and β = 124.1528° [22]) exhibiting several symmetric variants of an orientation relationship within a δ matrix. A simulation of this diffraction pattern is shown in Fig. 2(h), in which reflections from the δ phase are shown in black and the four orientation variants of the monoclinic Ag_2Te phase [22] are shown in blue, green, red, and purple. The orientation relationships are defined as:

$$\begin{aligned} &\mathrm{OR1}: [001](200)_\delta \,||\, [021](11\bar{2})_{Ag2Te} \rightarrow \textit{green} \\ &\mathrm{OR2}: [001](020)_\delta \,||\, [021](11\bar{2})_{Ag2Te} \rightarrow \textit{blue} \\ &\mathrm{OR3}: [001](200)_\delta \,||\, [\bar{2}0\bar{1}](11\bar{2})_{Ag2Te} \rightarrow \textit{red} \\ &\mathrm{OR4}: [001](020)_\delta \,||\, [\bar{2}0\bar{1}](11\bar{2})_{Ag2Te} \rightarrow \textit{purple} \end{aligned} \tag{2.2}$$

The interpretation of this pattern as a two-phase mixture of monoclinic Ag_2Te and δ provides a more reasonable explanation of the diffraction pattern. One distinguishing feature between the tetragonal and two-phase simulations of the diffraction pattern is that the reflections labeled d, e, and f in Fig. 2.2(b) should be collinear for a tetragonal structure, but offset for Ag_2Te. Since they are not collinear, the data is consistent with the two-phase diffraction pattern simulation. The combined signal from the dark-field images should also completely fill space if the tetragonal simulation is correct; this is not the case. A simulation of the multiple variants of Ag_2Te precipitates in δ, like the one shown in Fig. 2.2(h), is consistent with the observed diffraction pattern in Fig. 2.2(b).

Data from larger-scale microstructural features is presented in the next sections to provide more direct compositional and structural evidence that the two phases present in the microstructure are the rocksalt δ phase and the monoclinic Ag_2Te phase. The

similarities in the diffraction patterns and the orientation relationships between the fine-scale and larger-scale features suggest that they are both the result of the same two-phase mixture.

Composition and structure of the matrix phase

Diffraction and chemical analysis confirmed that the matrix phase is a Sb-enriched, rocksalt structure. Surveys of the sample at lower magnification identified some regions without second-phase precipitates in which the matrix phase could be analyzed directly. Based on the phase diagram (Fig. 2.1), the δ phase should be enriched in Sb and depleted in Ag by several atomic percent relative to 25 at. %. Compositional measurements of the matrix phase using electron microprobe yielded a composition of 22 at. % Ag, 28 at. % Sb, and 50 at. % Te, consistent with such an enrichment, the δ phase boundaries of the phase diagram, and within experimental error of measurements from previous work ($Ag_{19}Sb_{29}Te_{52}$) [23]. Similar results were obtained (within 1 at. %) from EDS measurements in the TEM.

Several zone axis diffraction patterns were obtained and compared to the proposed structures for $AgSbTe_2$, including the rocksalt structure originally proposed by Geller and Wernick [14] and several alternative structures recently proposed by Quarez et al.[15]. Representative diffraction patterns from the matrix phase are shown in Fig. 2.3(a). As summarized in the table in Fig. 3(a), these diffraction observations are consistent with the rocksalt structure. Simulations of the proposed ordered structures, including ordered tetragonal, cubic, and trigonal structures, did not reproduce the diffraction patterns observed for the matrix phase. We calculated electron diffraction patterns for these different structures and found, in each case, that the ordering produces additional reflections (a reflection corresponding to a 4.29 Å d-spacing, as one example) that are not present in our measured diffraction patterns from the matrix phase.

Composition and structure of the precipitate phase

Electron microprobe and diffraction analyses on larger volumes of the precipitate phase confirmed the presence of monoclinic Ag_2Te. Some regions of precipitate phase were large enough to be measured and analyzed independently from the matrix phase. The composition of the Ag-rich lamellae was 67 at. % Ag and 33 at. % Te (less than 1 at. % Sb), as measured by electron microprobe. As the molten ingot is cooled below 575 °C, it goes through a two-phase δ + L region in the phase diagram. At 548 °C, the remainder of the liquid phase is enriched in Ag (40 at. % Ag) and undergoes eutectic solidification. The final stage of the solidification process produces relatively large, 10-μm-wide, alternating lamellae from which independent diffraction and chemical analysis on each phase in the two-phase mixture was obtained (images of these features can be found in the literature, e.g. [18, 24]).

A number of diffraction patterns from the lamellae were obtained to establish the orientation relationships of the lamellae with respect to the matrix. The lamellae always preserved one of the OR variants in Eq. 2.2. Selected-area diffraction patterns of these lamellae are shown in Fig. 2.3(a). The diffraction patterns could be indexed consistently

according to the monoclinic structure[22]. Both the composition and diffraction data confirmed the presence of monoclinic Ag_2Te. As shown in Fig. 2.2(h), observed diffraction patterns, like those shown in Fig. 2.2(b) with "extra" reflections, can be explained as a two-phase mixture of cubic δ phase with fine-scale monoclinic Ag_2Te precipitates having the orientation variants defined in Eq. 2.2. These smaller precipitates likely formed while the sample was cooled between 548 °C and 360 °C as a result of a supersaturation of Ag in δ rather than from eutectic solidification. This interpretation of the data is consistent with the chemical and diffraction analysis.

Additional chemical analysis was performed on ≈100-nm-wide ligaments of the precipitate material that likely formed as secondary branches of the lamellae during eutectic solidification. The corresponding BF and DF images of Fig. 3(b) and (c) show examples of these ligaments. When a reflection for one monoclinic variant is chosen to create the DF image in (c), then only the regions of the precipitate exhibiting that specific crystallographic orientation variant become bright. The bright and dark bands in the precipitate BF and DF images correspond to domains of different orientation variants of the monoclinic structure. Corresponding EDS spectra for the precipitate (blue) and matrix (red) are shown in Fig. 3(d). The measured intensity ratios from the EDS spectra of AgLα/TeLα are 1.2 in the precipitate versus 0.72 in the matrix, indicating a precipitate enriched with Ag. It was not possible to isolate the signal from these 100-nm-wide ligaments because they were embedded in the matrix. Although the phase diagram suggests that a eutectoid reaction occurs at 360 °C in which Sb_2Te_3 precipitates form, there was no evidence of Sb_2Te_3 precipitates in the observed microstructure. The formation of Sb_2Te_3 precipitates may have been suppressed by a sufficiently fast cooling rate, ≈3°/min to 150 °C and 0.7°/min to room temperature, as power to the furnace was simply turned off. However, previous experiments [19, 25] on similar systems failed to reproduce the eutectoid reaction that was reported by Offergeld et al. [18] and Stegherr et al. [26]. The microstructural data in this study is consistent with the presence of only Ag_2Te and δ.

2.1.4 Origin and Significance of the Orientation Relationship

The diffraction and chemical analysis presented in earlier sections demonstrated the existence of an orientation relationship between monoclinic Ag_2Te and δ. The origin and significance of this orientation relationship are now discussed. It will be shown that the precipitation of Ag_2Te begins with the close alignment of the Te sublattices in both phases at elevated temperature. Above 145 °C, the equilibrium phase of Ag_2Te has a cubic crystal structure, with Te atoms occupying the fcc positions and four Ag atoms at the 1/4 1/4 1/4 positions to form a zincblende structure with the anions, while the other four Ag atoms are distributed statistically over a large number of lattice positions[22]. The lattice parameter of the cubic phase varies with temperature and has been reported as 6.6808 Å at 650 °C [22]. Studies of the cubic-to-monoclinic phase transformation in Ag_2Te showed that the monoclinic basis vectors a, b, and c have a simple relationship to the cubic basis vectors $\mathbf{a}_1$, $\mathbf{a}_2$, and $\mathbf{a}_3$[21]:

$$\begin{aligned}\mathbf{a} &= \tfrac{1}{2}(\mathbf{a}_1 - \mathbf{a}_2) + \mathbf{a}_3 \\ \mathbf{b} &= \tfrac{1}{2}(\mathbf{a}_1 + \mathbf{a}_2) \\ \mathbf{c} &= \mathbf{a}_2 - \mathbf{a}_1\end{aligned} \tag{2.3}$$

Fig. 2.4(a) shows schematically the ideal relationship between the cubic and monoclinic crystal structures. In this figure, only the positions of the Te atoms are shown. The monoclinic unit cell is shown in red, and its relationship to the cubic unit cell is visible in the figure. Small displacements of the Te atoms from the perfect positions of the cubic lattice create the monoclinic structure. This type of displacive transformation can occur rapidly because it does not require diffusion. Thus, the cubic phase is not likely to be kinetically stabilized at room temperature, which explains why it is not observed. The calculated distortions in the monoclinic phase from the ideal fcc structure are ε_a = −0.94%, ε_b = 4.5%, ε_c = 4.0%, ε_α = 0%, ε_β = 0.89% and ε_γ = 0%. Previously, the orientation relationship between the cubic and monoclinic Ag_2Te phase was defined as [21]:

$$\begin{aligned}&[001]_{cubic} \parallel [201]_{monoclinic} \\ &[010]_{cubic} \parallel [021]_{monoclinic} \\ &[100]_{cubic} \parallel [02\bar{1}]_{monoclinic}\end{aligned} \tag{2.4}$$

The orientation relationship between δ and monoclinic Ag_2Te defined in Eq. (2.2) is symmetrically equivalent to the orientation relationship between cubic and monoclinic Ag_2Te. A generalized version of this relationship is (<u v w> and {h k l} represent families of symmetrically equivalent directions and planes, respectively):

$$\begin{aligned}&<100>_\delta \parallel \pm[021];\pm[\bar{2}0\bar{1}];\pm[02\bar{1}]_{\mathrm{Ag2Te}} \\ &\{010\}_\delta \parallel (\bar{1}12);(11\bar{2})_{\mathrm{Ag2Te}}\end{aligned} \tag{2.5}$$

There are a total of twelve possible symmetric variants (6 parallel zone axes × 2 parallel sets of planes = 12 variants) for the monoclinic-to-cubic orientation relationship. Schematics that illustrate additional orientation variants obtained by 90° rotations about cubic axes are shown in Fig. 2.4(b)–(d). These operations generate the four orientation variants in Eq. (2). Operations with additional rotation symmetry operators produce all twelve variants.

The crystallographic alignment between the monoclinic phase and δ at room temperature suggests that the two phases must be aligned at elevated temperature also. As a result, it can be inferred that the cubic phase of Ag_2Te is topotactically aligned with the δ phase in a cube-on-cube orientation at elevated temperature even though the lattice misfit between the two cubic phases is relatively high (approximately 8–10%). The cubic Ag_2Te phase can form topotactically on the already present Te sublattice in δ by rearranging Ag atoms and displacing Sb atoms. The extent of diffusion required for the phase transformation is greatly reduced because the Te is already positioned on the appropriate lattice sites for the new phase. In this way, the Te sublattice in the δ phase provides a nucleation template for the cubic Ag_2Te phase and its formation occurs

without an energetically costly transformation event. A displacive transformation then provides an easy route to the monoclinic structure. This sequence of incremental microstructural changes leads the final microstructure observed at room temperature.

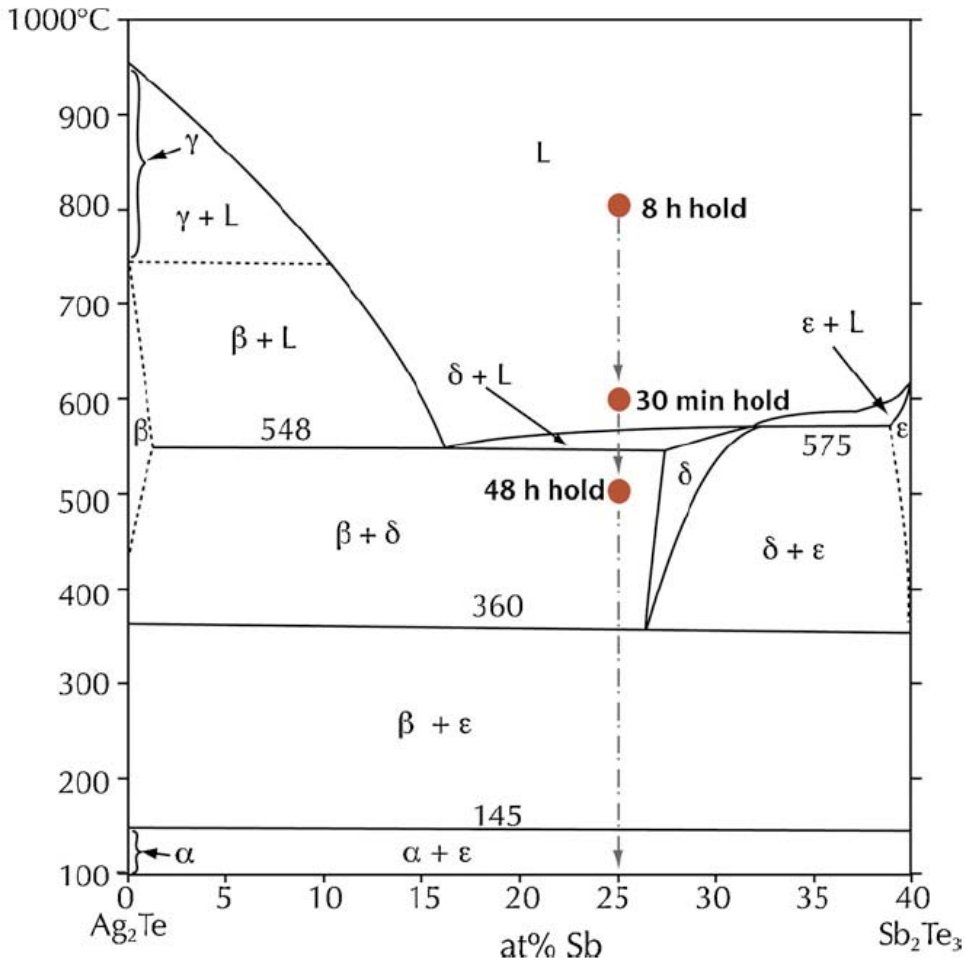

Figure 2.1 Pseudobinary Ag_2Te–Sb_2Te_3 slice of the ternary Ag–Sb–Te phase diagram[13]. The rocksalt $AgSbTe_2$ phase is only stable in the region marked δ. Note that there exists considerable disagreement in the literature concerning the exact phase boundaries for the δ region (see text). Below 145 ◦C, the cubic β-Ag_2Te phase transforms into the monoclinic α-Ag2Te phase. Each phase is identified with a Greek letter: (α)monoclinic Ag2Te, (β) face-centered cubic Ag_2Te, (γ) body-centered cubic Ag_2Te, and (ε) trigonal Sb_2Te_3. The dot-dash grey arrows identify the thermal treatment of the sample in this study.

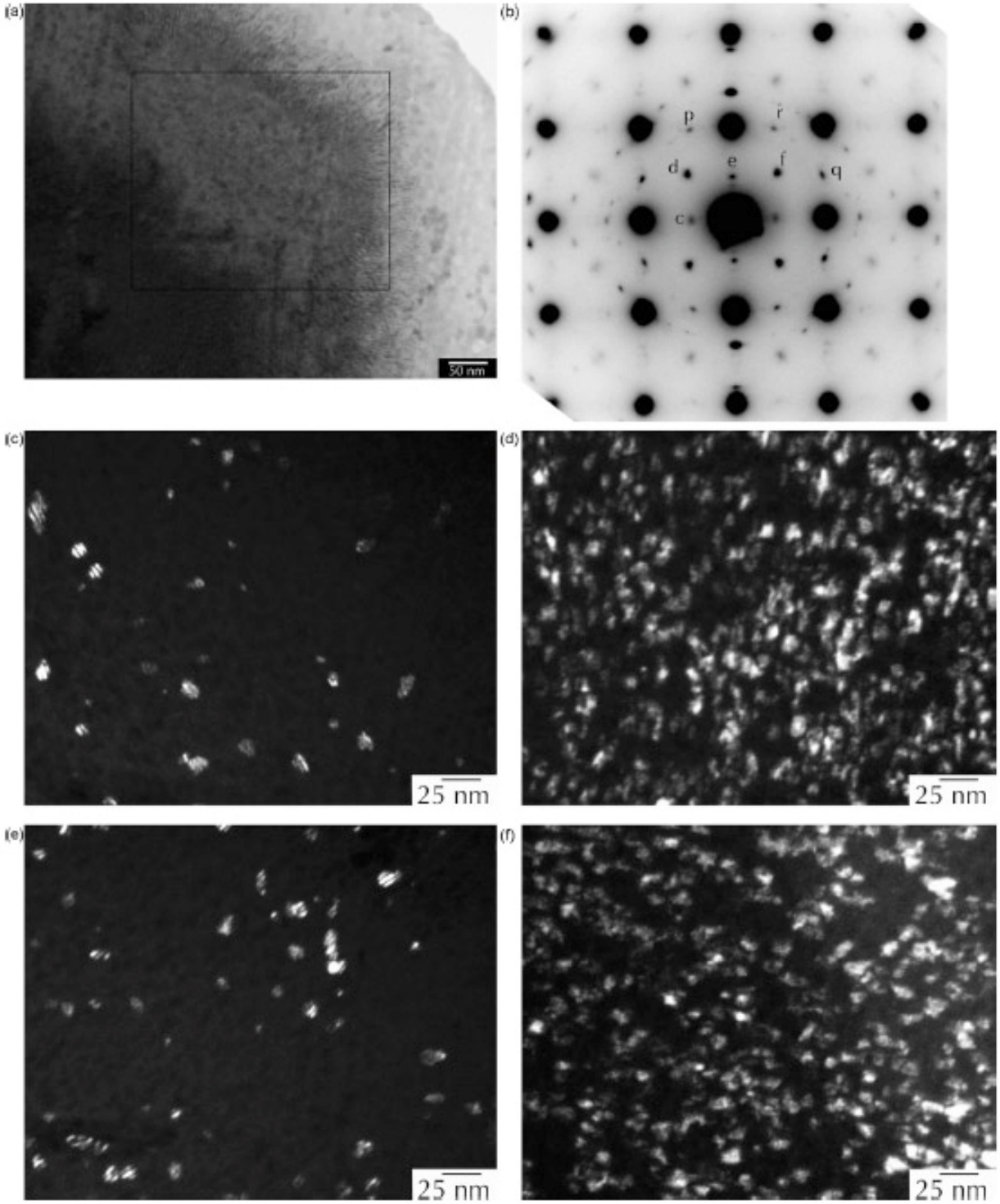

Figure 2.2 (a-f) see next page for caption.

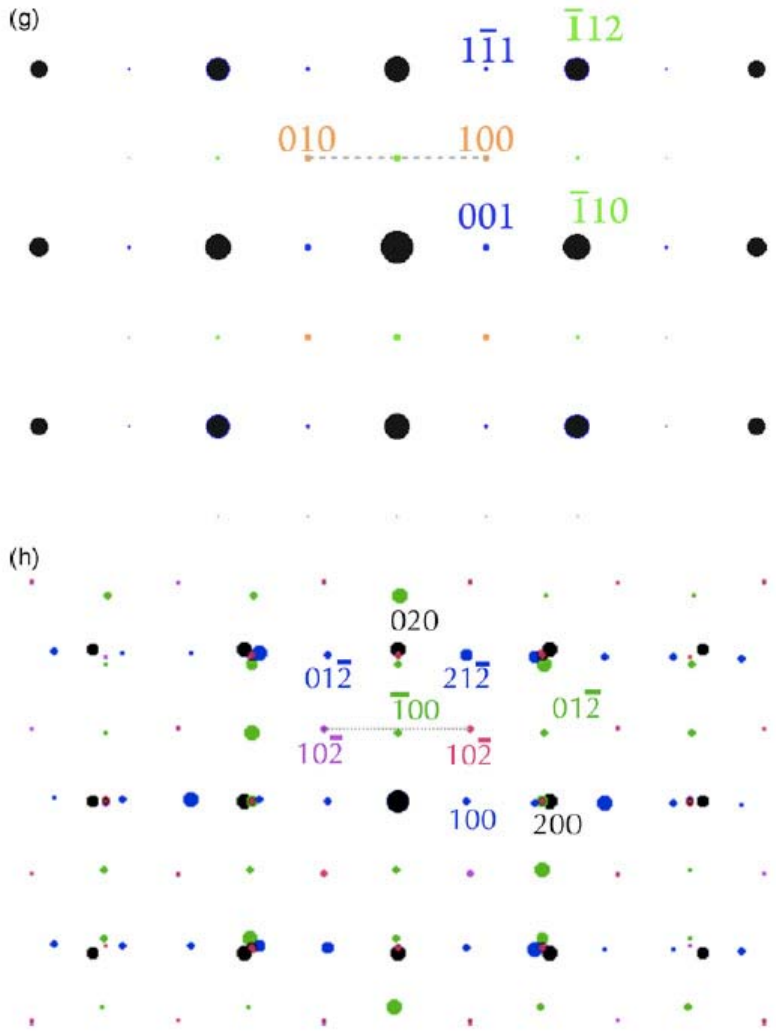

Figure 2.2 (see a-f on preceding page). Bright-field image (a) of a solidified ingot in a [0 0 1] zone axis orientation with dotted lines marking the region used for the higher-magnification dark-field images in (c)–(f). Corresponding diffraction pattern (b) with extra reflections that do not belong to a disordered rocksalt structure are labeled c, d, e, f, p, q, and r. Each image (c)–(f) corresponds to its respective extra reflection in (b). A comparison between simulated zone axis diffraction patterns for (g) three variants of the tetragonal structure (orange, blue, green, and black for reflections shared by all variants), and (h) four orientation variants of a monoclinic Ag_2Te (purple, red, blue, and green) phase in a cubic, δ (black) matrix show that (h) is the more likely possibility because d, e, and f in (b) are not collinear.

(a)

	Zone Axis	*hkl*	$d_{measured}$ (Å)	$d_{calculated}$ (Å)	Diffraction Pattern
δ phase: rocksalt structure	$[001]$	020	3.04	3.04	
		220	2.15	2.15	
		240	1.36	1.36	
		420	1.35	1.36	
	$[0\bar{1}1]$	$\bar{2}00$	305	3.04	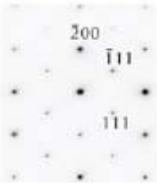
		$\bar{1}11$	3.50	3.51	
		022	2.13	2.15	
		$\bar{3}11$	1.83	1.83	
		$\bar{4}22$	1.23	1.24	
	$[1\bar{1}2]$	$1\bar{1}\bar{1}$	3.50	3.51	
		$\bar{2}\bar{2}0$	2.16	2.15	
		$\bar{3}\bar{1}1$	1.82	1.83	
		$\bar{4}02$	1.35	1.36	
	$[1\bar{1}3]$	$\bar{2}\bar{2}0$	2.15	2.15	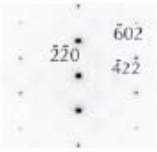
		$\bar{6}02$	0.956	0.961	
		$\bar{4}22$	1.24	1.24	
Ag_2Te: monoclinic	$[0\bar{2}1]$	$\bar{1}00$	6.76	6.75	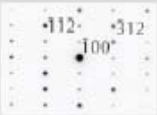
		$\bar{1}12$	3.19	3.17	
		$\bar{2}12/0\bar{1}\bar{2}$	2.86/2.84	2.88/2.86	
		$\bar{3}12/\bar{1}\bar{1}\bar{2}$	2.32/2.29	2.32/2.30	
	$[0\bar{1}0]$	100	6.76	6.75	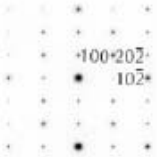
		$\bar{1}02$	4.47	4.49	
		$20\bar{2}/002$	3.71/3.71	3.76/3.71	
		$30\bar{2}/102$	2.70/2.68	2.72/2.68	
	$[\overline{412}]$	$10\bar{2}$	4.48	4.49	
		$02\bar{1}/1\bar{2}\bar{1}$	2.13/2.13	2.14/2.14	
		$12\bar{3}/2\bar{2}\bar{3}$	1.76/1.78	1.77/1.78	
		$22\bar{5}/3\bar{2}\bar{5}$	1.38/1.39	1.39/1.39	

Figure 2.3a Measured *d*-spacings from several indexed high-symmetry zone axes and corresponding diffraction patterns from matrix and precipitate phase. Interplanar spacings were calculated from crystallographic information contained in refs. [14] and [22]. The diffraction data is consistent with the rocksalt structure, for which Ag and Sb are distributed randomly on the cation sublatttice, and the monoclinic Ag_2Te phase..

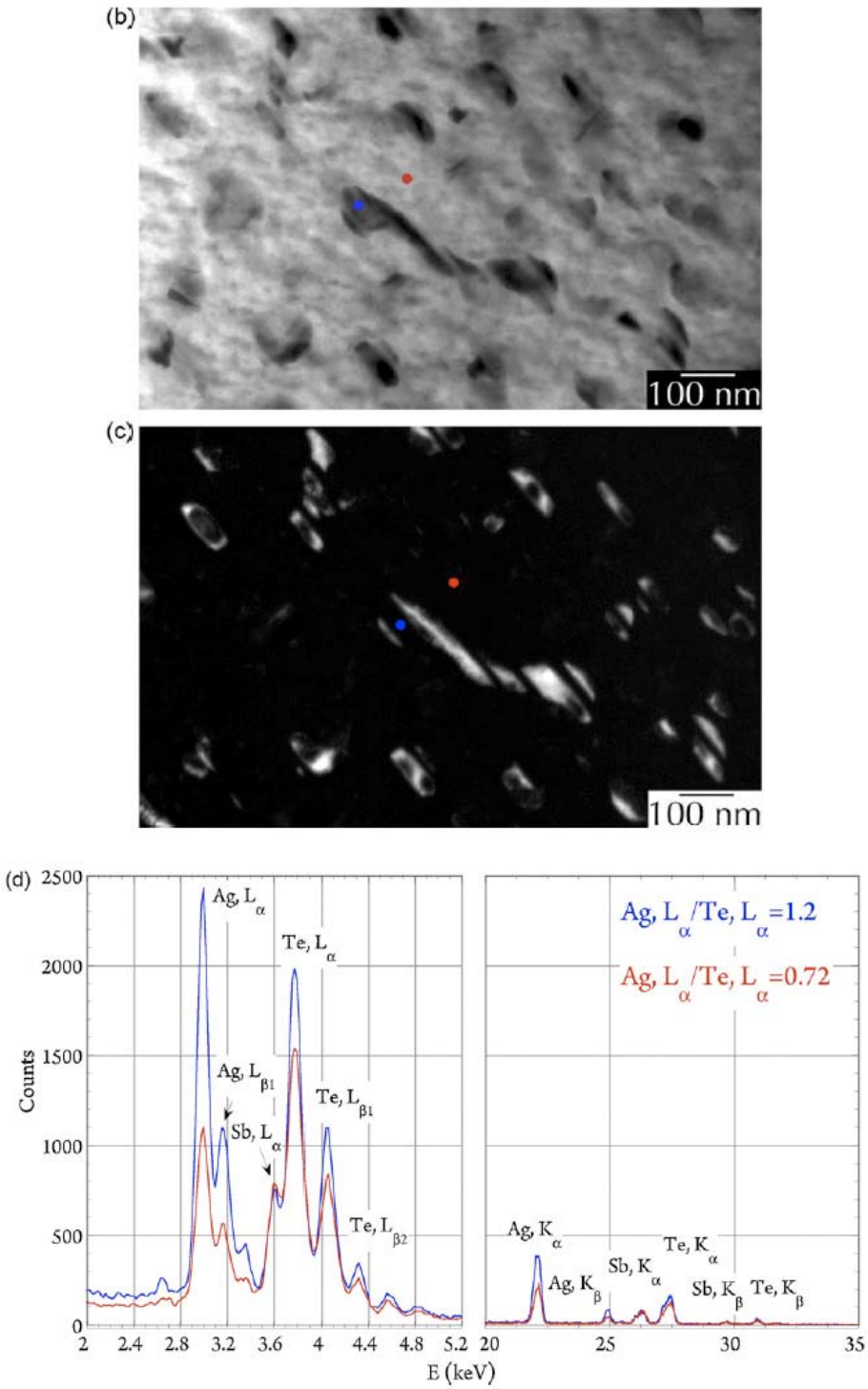

Figure 2.3(b-d) Corresponding (b) BF and (c) DF images of secondary branches of lamellae that formed during eutectic solidification. The intensity of the EDS spectra in (d) of the blue and red points shown in (b) and (c) shows that the precipitate is enriched in Ag. The intensity ratio of $AgL_{\alpha}/TeL_{\alpha}$ is 1.2 in the precipitate, compared to 0.72 in the matrix. Accurate compositional quantification is not possible because the precipitates are embedded in the matrix.

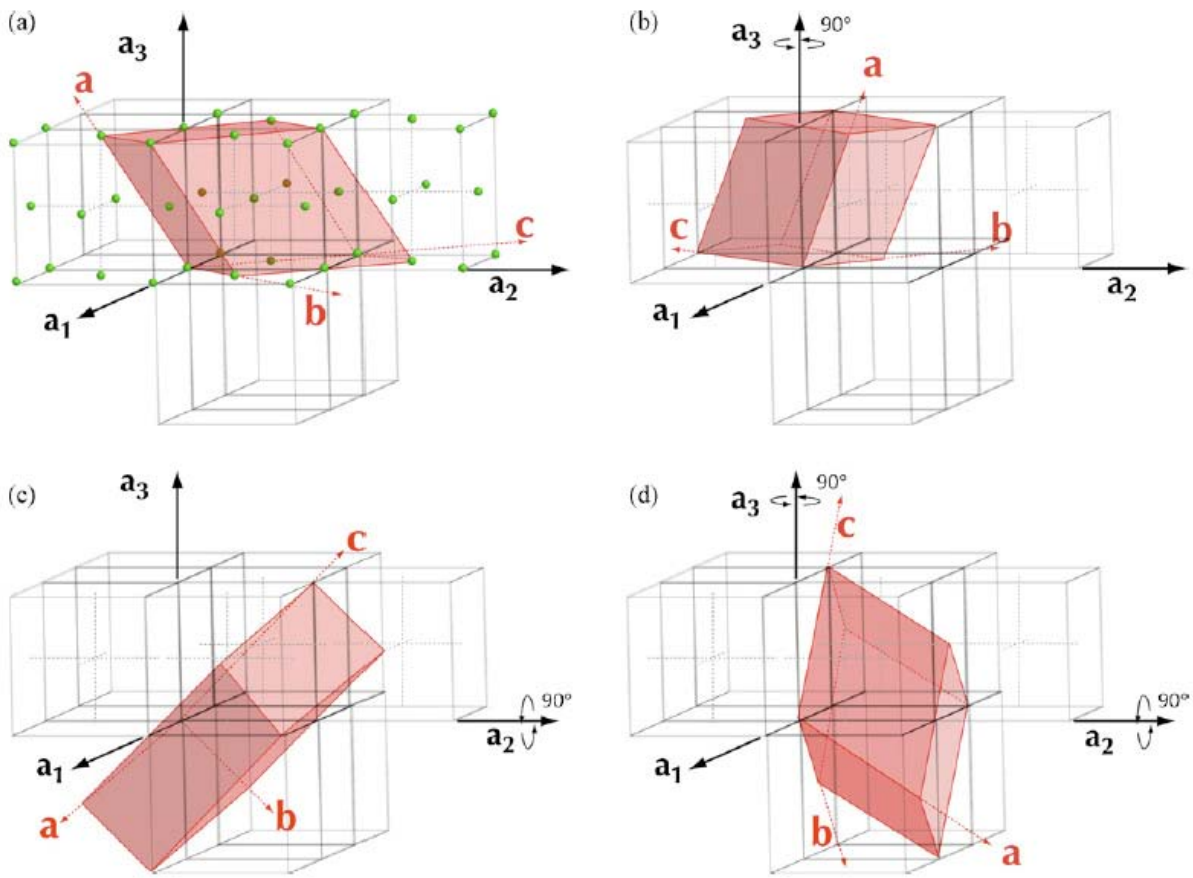

Figure 2.4 (a) Schematic showing the relationship between the cubic basis vectors $\mathbf{a_1}$, $\mathbf{a_2}$, and $\mathbf{a_3}$ and the monoclinic basis vectors **a**, **b**, and **c** of Ag_2Te. Only the Te atoms are shown. Small displacements of the Te atoms relative to the ideal cubic structure shown in (a) occur rapidly during the diffusionless transformation at 145◦C and result in the observed monoclinic structure. The monoclinic unit cell is shown in red. Three other symmetric variants, which are shown in (b), (c), and (d), are related to (a) by a 90◦rotation about $\mathbf{a_3}$, a 90◦ rotation about $\mathbf{a_2}$, and a 90◦ rotation about $\mathbf{a_2}$ followed by a 90◦ rotation about $\mathbf{a_3}$, respectively. There are a total of 12 symmetric variants of the orientation relationship.

2.2 Interfacial Defect Structure at Sb_2Te_3 Precipitates in $AgSbTe_2$

It is also useful to consider interfaces between rocksalt structured tellurides, such as in PbTe [5]and $AgSbTe_2$ [6], and tetradymite structured tellurides[8], such as Bi_2Te_3 and Sb_2Te_3 [7]. That such compounds consist of similar stackings of close-packed metal and chalcogen layers (see Fig. 2.5) suggests the possibility of forming well-ordered coherent or semicoherent heterophase interfaces. This notion has motivated recent interest in combining rocksalt and tetradymite-structured tellurides as nanocomposites, with the goal of improving thermoelectric properties by using high densities of embedded interfaces to reduce thermal conductivity through increased phonon scattering [4]. One route to producing such multi-phase thermoelectric structures is through solid-state phase transformations. For instance, recent work has explored the growth of lamellar PbTe/Sb_2Te_3 nanocomposites through control of eutectoid decomposition reactions and solid-state precipitation [27-30].

In this section, we investigate an interface between $AgSbTe_2$ and Sb_2Te_3 to gain insight concerning the transformation mechanism between these rocksalt and tetradymite structured tellurides. We use high-resolution transmission electron microscopy (HRTEM) to analyze a line defect at the {111}$AgSbTe_2$/(0001)Sb_2Te_3 interface. From this analysis we discuss the role that such defects may play in the growth of the tetradymite-structured precipitates within rocksalt structured tellurides.

2.2.1 Experimental procedure

To study the interface between Sb_2Te_3 and $AgSbTe_2$, we prepared an ingot by melting elemental constituents in an appropriate ratio and then solidifying and annealing this material. We chose a composition of 16.7 at % Ag, 30.0 at % Sb, and 53.3 at % Te. This composition falls on the Ag_2Te-Sb_2Te_3 pseudo-binary section of the Ag-Sb-Te ternary phase diagram [13, 18, 19] and corresponds to a composition of x=0.642 in the formula $(Ag_2Te)_{1-x}(Sb_2Te_3)_x$. As noted in section 2.1, the single-phase rocksalt phase "$AgSbTe_2$" exists over a range of stoichiometries. For large enrichments of the Sb_2Te_3 mole-fraction, cooling from the solid-solution region yields plates of Sb_2Te_3 that lie parallel with the {111} planes of the rocksalt phase [16, 19]. Our goal was to create a compound that could be supersaturated in Sb_2Te_3 at elevated temperature such that a solid-state precipitation reaction would occur at reduced temperature to form a two-phase mixture. The composition we chose for our samples is significantly enriched in Sb_2Te_3 such that it is possible to form a supersaturated "$AgSbTe_2$" rocksalt compound at elevated temperature and precipitate Sb_2Te_3 in the solid state at reduced temperature.

The elemental constituents, in pellet form (99.999% Ag, 99.9999% Sb and Te, Alfa Aesar) were loaded into a quartz ampoule that was then evacuated to a pressure less than 10^{-7} Torr and sealed. We chose a thermal treatment to precipitate Sb_2Te_3 following the phase-diagram as assessed by Maier [13]. This treatment consisted of melting and holding the material at 850°C for 3.5 h with gentle agitation three times over this period; solution annealing the material in the single-phase rocksalt "$AgSbTe_2$" region of the phase diagram at 552°C for 112 h; and, finally, annealing the material in the two-phase $AgSbTe_2$+Sb_2Te_3 region of the phase diagram at 500°C for 4.5 h. Following each of these steps the material was quenched into iced brine. After annealing for 112 h at 552°C, a

powder XRD diffraction pattern confirmed that all peaks belonged to the $AgSbTe_2$ phase. Only after the anneal at 500°C was the formation of a second phase detected, which is consistent with a solid-state precipitation reaction. Specimens for TEM analysis were prepared by mechanical dimpling, followed by argon ion milling using a liquid-nitrogen-cooled stage. Electron microscopic observations were conducted in a 200kV JEOL 2010F TEM and a 400 kV JEOL 4000EX HRTEM.

2.2.2 Results and Discussion

Lower magnification observations of the microstructure following annealing showed the formation of plate-like precipitates of the Sb_2Te_3 phase. A TEM image of these plates is shown in Fig. 2.6. Selected area electron diffraction shows that the plates are oriented with $\{0001\}_{Sb_2Te_3} \parallel \{111\}_{AgSbTe2}$ and $<2\bar{1}\bar{1}0>_{Sb_2Te_3} \parallel <110>_{AgSbTe2}$. This orientation relationship aligns the close-packed planes and directions in both phases. These plates are similar in morphology and orientation relationship to the Sb_2Te_3 plates in PbTe recently analyzed by Ikeda et al. [29].

We observed atomic-scale steps along the interface. An HRTEM image of one such step is shown in Fig 2.7. Interfacial defects with step and dislocation content, termed interfacial "disconnections"[31], play important roles in many solid-state phase transformations. A critical question is what role such defects play in the atomic rearrangements required for the transformation from rocksalt to tetradymite to occur. To address this question, we analyzed the geometrical and dislocation properties of this defect.

We employed the formalism developed by Pond and Hirth [32, 33] to analyze the defect by a circuit mapping procedure. The Burgers vector of a line defect at an interface between two crystals, λ and μ, can be determined by circuit-mapping from: $\mathbf{b} = -[\mathbf{C}(\lambda) + \mathbf{PC}(\mu)]$, where $\mathbf{C}(\lambda)$ and $\mathbf{C}(\mu)$ are the segments of the circuit in the λ and μ crystals and $\mathbf{P}$ is a matrix that transforms a vector from the crystal coordinates of μ to those of λ. In our case, we take $AgSbTe_2$ and Sb_2Te_3 as λ and μ, respectively. Figure 2.7 shows the circuit elements determined from the HRTEM image and gives the values for $\mathbf{C}(\lambda)$ and $\mathbf{C}(\mu)$. To define the Burgers vector, we chose a reference state for which the $(0001)_{Sb2Te3}$ and $\{111\}_{AgSbTe2}$ planes are aligned and strained into coherency. With this consideration, and for the coordinate system defined here, $\mathbf{P}$ is obtained from:

$$\mathbf{P} = \mathbf{LAM} = \begin{pmatrix} \frac{-1}{\sqrt{2}} & \frac{1}{\sqrt{6}} & \frac{1}{\sqrt{3}} \\ 0 & \frac{-2}{\sqrt{6}} & \frac{1}{\sqrt{3}} \\ \frac{1}{\sqrt{2}} & \frac{1}{\sqrt{6}} & \frac{1}{\sqrt{3}} \end{pmatrix} \begin{pmatrix} r & 0 & 0 \\ 0 & r & 0 \\ 0 & 0 & 1 \end{pmatrix} \begin{pmatrix} 1 & \frac{-1}{2} & 0 \\ 0 & \frac{\sqrt{3}}{2} & 0 \\ 0 & 0 & \xi \end{pmatrix} = \begin{pmatrix} \frac{-r}{\sqrt{2}} & \frac{r}{\sqrt{2}} & \frac{\xi}{\sqrt{3}} \\ 0 & \frac{-r}{\sqrt{2}} & \frac{\xi}{\sqrt{3}} \\ \frac{r}{\sqrt{2}} & 0 & \frac{\xi}{\sqrt{3}} \end{pmatrix} \qquad (2.6)$$

Here, **M** converts from μ crystal coordinates to unit orthogonal coordinates, **A** brings μ and λ into coherency, and **L** converts from unit orthogonal coordinates to λ crystal coordinates. Finally, r is the ratio of distances between close-packed atoms in the rock-salt and tetradymite phases (i.e., $r = a_{cub}/\sqrt{2}a_{hex}$=1.008) and ξ is the c/a ratio in the tetradymite phase (ξ=7.136). (Note that in this equation, the directions in the tetradymite phase are expressed in three-index rather than four-index notation). Table 1 summarizes the Burgers vector and step character of the defect analyzed in Fig. 2.7.

The physical significance of this defect can be understood by considering the relationship between the rocksalt and tetradymite structures. Frangis and co-workers have previously discussed similarities between rock-salt and tetradymite chalcogenide compounds of the general form MX and M_2X_3 [34]. As they discuss, the stacking sequences of the close packed planes in these structures (i.e. (0001) and {111} in the M_2X_3 and MX structures, respectively) can be represented symbolically as:

$$A\beta C\ \alpha B\gamma\ A\beta C\ \alpha B\gamma\ A\beta C\ \alpha B\gamma\ \ldots\ (MX) \qquad (2.7a)$$

$$A\beta C\alpha B\ C\alpha B\gamma A\ B\gamma A\beta C\ \ldots \qquad (M_2X_3) \qquad (2.7b)$$

In this representation, the Roman letters (A,B,C) represent the chalcogenide layers (e.g. Te, Se), the Greek characters represent the metal layers, and each increment in either the Roman or Greek alphabet represents a lateral displacement of the layer by a vector of type $\frac{1}{3}<10\bar{1}0>$ (or equivalently $\frac{1}{6}<121>$ relative to the cubic crystal system).

These layers are labeled accordingly in the schematics of the MX and M_2X_3 structures shown in Fig. 2.5. The essential difference between the two structures is the following: in the MX structure, the layers alternate between metal and chalcogen layers throughout the structure, whereas, in the M_2X_3 structure, two adjacent chalcogen layers arise every five planes within the sequence. The M_2X_3 structure can thus be generated from the MX structure by removing every 6th metal plane, closing the resulting gap, and shearing each remaining 5-layer block laterally to restore the correct stacking sequence.

The interfacial disconnection that we have observed here provides a means to accomplish this series of operations. To see this, it is helpful to decompose the Burgers vector into components normal and parallel to the interface plane (see Table 1). The normal component, $\mathbf{b}_{\perp}$, arises from the difference in step heights in the two crystals. In the $AgSbTe_2$ crystal (λ) this step corresponds to 6 close-packed planes ($h_{\lambda} = \sqrt{3}a_{cub}$), whereas in the Sb_2Te_3 crystal (μ) the step consists of 5 close-packed planes ($h_{\mu} = c_{hex}/3$). As illustrated schematically in Figure 4, this difference in step heights is consistent with that expected for removal of one of the close-packed metal planes from the rock-salt phase by dislocation climb. This process on its own would produce two adjacent layers

of Te atoms, but these layers would be left in the wrong stacking sequence. As shown in Figure 4(b), motion of the parallel component of the disconnection, $\mathbf{b}_{\parallel} = a_{cub}/6[\bar{1}2\bar{1}]$, which is analogous to a Shockley partial dislocation, shears these layers into the correct stacking sequence, thereby moving the rocksalt/tetradymite interface up to this plane.

Growth of the Sb_2Te_3 plate requires a net influx of Sb and rejection of Ag. (Although some Ag is soluble in Sb_2Te_3, our microprobe measurements indicate that this is less than 1 at. % Ag is present in Sb_2Te_3 at equilibrium). The atomic flux for motion of the disconnection can be quantified from its geometrical properties using the theory developed by Hirth and Pond [33]. Specifically, the number of atoms of species i, ΔN_i, required to move a length of disconnection, L, by a distance along the interface, δy, can be determined from:

$$\frac{\Delta N_i}{L\delta y} = \left(X_i^{\lambda} - X_i^{\mu}\right)h + X_i^{\lambda} b_{\perp} \qquad (2.8)$$

where h is the overlap step height (in this case equal to $h_{\mu} = c_{hex}/3$) and $b_{\perp}$ is the normal component of the Burgers vector ($\sqrt{3}a_{cub} - c_{hex}/3$). In this expression, the left and right terms represent the fluxes associated, respectively, with the step and dislocation parts of the disconnection.

Table 2.2 shows the computed atomic fluxes required to move the disconnection for the simplified case in which the two phases are at the exact stoichiometries of $AgSbTe_2$ and Sb_2Te_3. Here, the flux of Te atoms associated with the dislocation and step parts of the disconnection are exactly opposite, and therefore cancel. Thus, long-range diffusive transport of Te is required for motion of the disconnection. In contrast, the Sb and Ag fluxes are largely associated with motion of the step part of the disconnection, with the total Ag flux being a factor three larger than the total Sb flux and oppositely signed. This analysis can be extended straightforwardly to more realistic compositions based on the actual bounds of the solid solution regions for the two phases, in which case the rock-salt phase is enriched in Sb and Te, while the tetradymite phase also has Ag and is deficient in Te. Under these more realistic conditions defect motion leading to growth the tetradymite plates would thus also require a net rejection of Te.

2.2.3 Conclusion

The type of analysis presented here should be generally applicable to other rock-salt/tetradymite telluride systems. In addition to providing insight concerning the transformation mechanism, the analysis of such defects should also help in understanding how misfit is accommodated at such interfaces. In the $AgSbTe_2/Sb_2Te_3$ system the {111}/(0001) misfit is reasonably small (~0.8%); however in other rock-salt/tetradymite telluride systems of interest, such as $PbTe/Sb_2Te_3$, the misfit can be much larger. An

improved understanding of the atomic mechanisms underpinning interface formation and stability in these systems should be useful in tailoring processes for forming thermoelectric nanocomposite of these materials and in understanding what controls their long-term stability.

Table 2.1. Summary of the geometrical properties of the observed disconnection at the $AgSbTe_2/Sb_2Te_3$ interface.

Burgers Vector:

$$\mathbf{b} = \left(\frac{5}{6} a_{cub} - \frac{c_{hex}}{3\sqrt{3}}, \quad \frac{8}{6} a_{cub} - \frac{c_{hex}}{3\sqrt{3}}, \quad \frac{5}{6} a_{cub} - \frac{c_{hex}}{3\sqrt{3}} \right) = \left(-0.7966, \quad 2.2424, \quad -0.7966\right) \mathring{A}$$

$$|\mathbf{b}| = 2.509 \ \mathring{A}$$

Normal Component:

$$\mathbf{b}_{\perp} = \left(a_{cub} - \frac{c_{hex}}{3\sqrt{3}} \right) [111]$$

$$|\mathbf{b}_{\perp}| = 0.3747 \ \mathring{A}$$

Parallel Component:

$$\mathbf{b}_{\parallel} = \frac{a_{cub}}{6} \left[\bar{1} 2 \bar{1} \right]$$

$$|\mathbf{b}_{\parallel}| = 2.481 \ \mathring{A}$$

Step Heights:

$$h_{\lambda} = \sqrt{3} a_{cub} = 10.527 \ \mathring{A} \qquad h_{\mu} = \frac{1}{3} c_{hex} = 10.152 \ \mathring{A}$$

The lattice parameters are $AgSbTe_2$: a_{cub}=6.078Å [14]; Sb_2Te_3: a_{hex}=4.264Å, c_{hex}=30.458Å [35]. λ refers to the $AgSbTe_2$ crystal and μ refers to the Sb_2Te_3 crystal. The Burgers vector is expressed relative to the λ crystal ($AgSbTe_2$) as oriented in Figure 2.7.

Table 2.2. Summary of the mass flux required for motion of the disconnection at the $AgSbTe_2/Sb_2Te_3$ interface.

Species	Step flux (atoms/Å^2)	Dislocation flux (atom/Å^2)	Total flux (atom/Å^2)
Ag	$\frac{2}{3}\frac{c_{hex}}{a_{cub}^3}$ +0.09043	$\frac{2}{a_{cub}^3}\left(\sqrt{3}a_{cub} - c_{hex}/3\right)$ +0.00334	$\frac{2\sqrt{3}}{a_{cub}^2}$ +0.09377
Sb	$\frac{2}{3}\frac{c_{hex}}{a_{cub}^3} - \frac{8\sqrt{3}}{3a_{cub}^2}$ -0.03459	$\frac{2}{a_{cub}^3}\left(\sqrt{3}a_{cub} - c_{hex}/3\right)$ +0.00334	$-\frac{2\sqrt{3}}{3a_{cub}^2}$ -0.03126
Te	$-\frac{4}{a_{cub}^3}\left(\sqrt{3}a_{cub} - c_{hex}/3\right)$ -0.00668	$+\frac{4}{a_{cub}^3}\left(\sqrt{3}a_{cub} - c_{hex}/3\right)$ +0.00668	0

In this table, we have chosen a sign convention for which a negative flux corresponds to transfer of atomic species *into* the defect for motion of the defect to the *left* with reference to Figure 2.7.

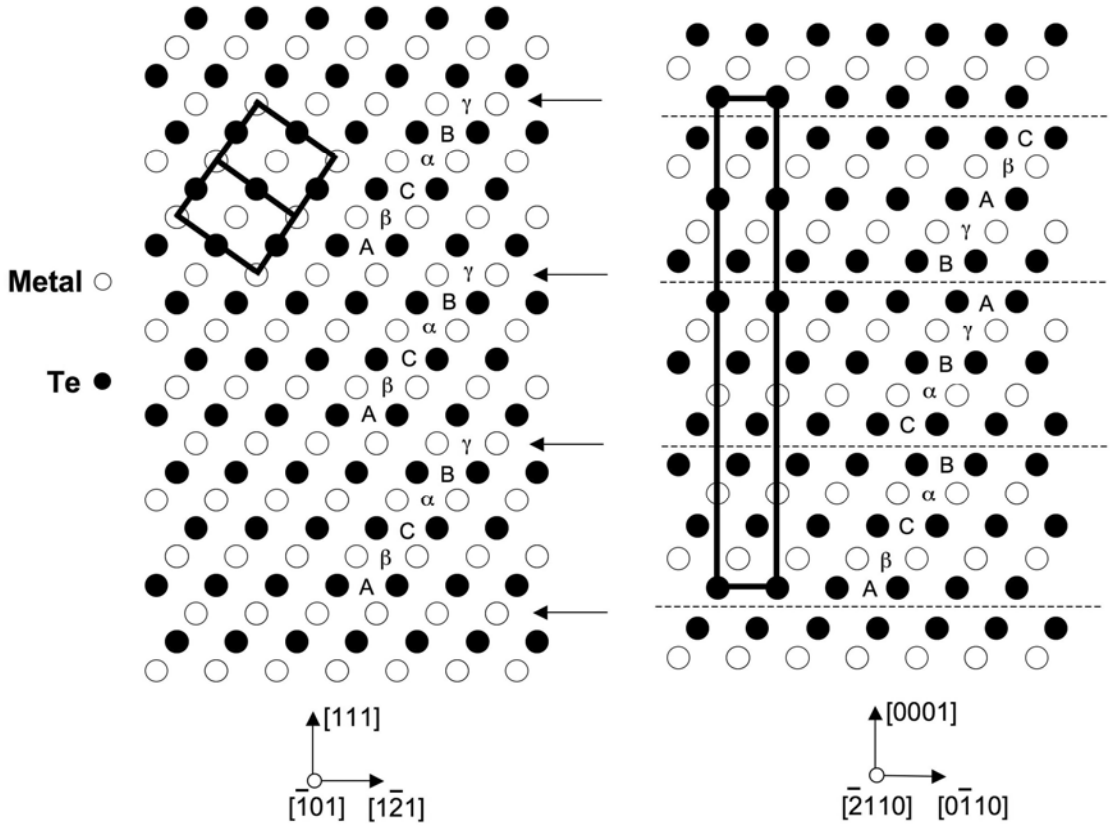

Figure 2.5. Schematic showing crystal structures for the (a) rock-salt and (b) tetradymite structured tellurides. The rocksalt structure (a) is projected along $[10\bar{1}]$ and the tetradymite structure (b) is projected along $[\bar{2}110]$. For both phases the stacking of the close-packed planes are given by the lettering with the metal (e.g. Ag, Sb) and tellurium planes indicated by Greek and Roman letters, respectively.

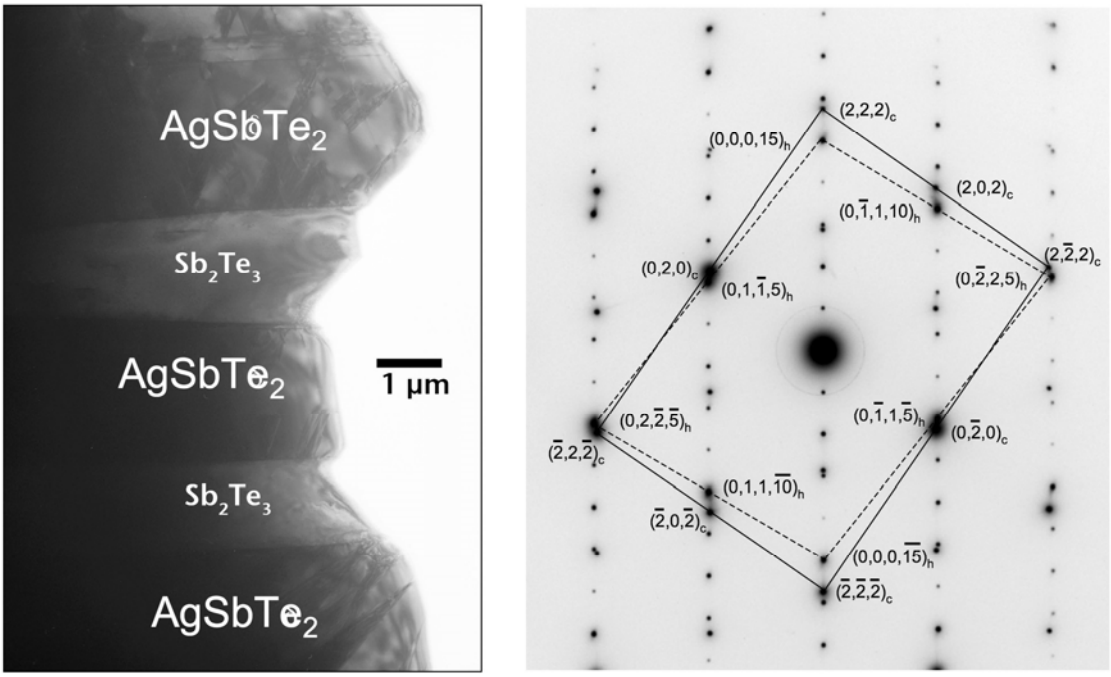

Figure 2.6. (a) TEM micrograph showing example of an Sb_2Te_3 plate in rock-salt $AgSbTe_2$ matrix. Electron diffraction (b) shows that these plates are oriented with $(0001)_{Sb_2Te_3} \parallel (111)_{AgSbTe_2}$ and $[\bar{2}110]_{Sb_2Te_3} \parallel [10\bar{1}]_{AgSbTe_2}$.

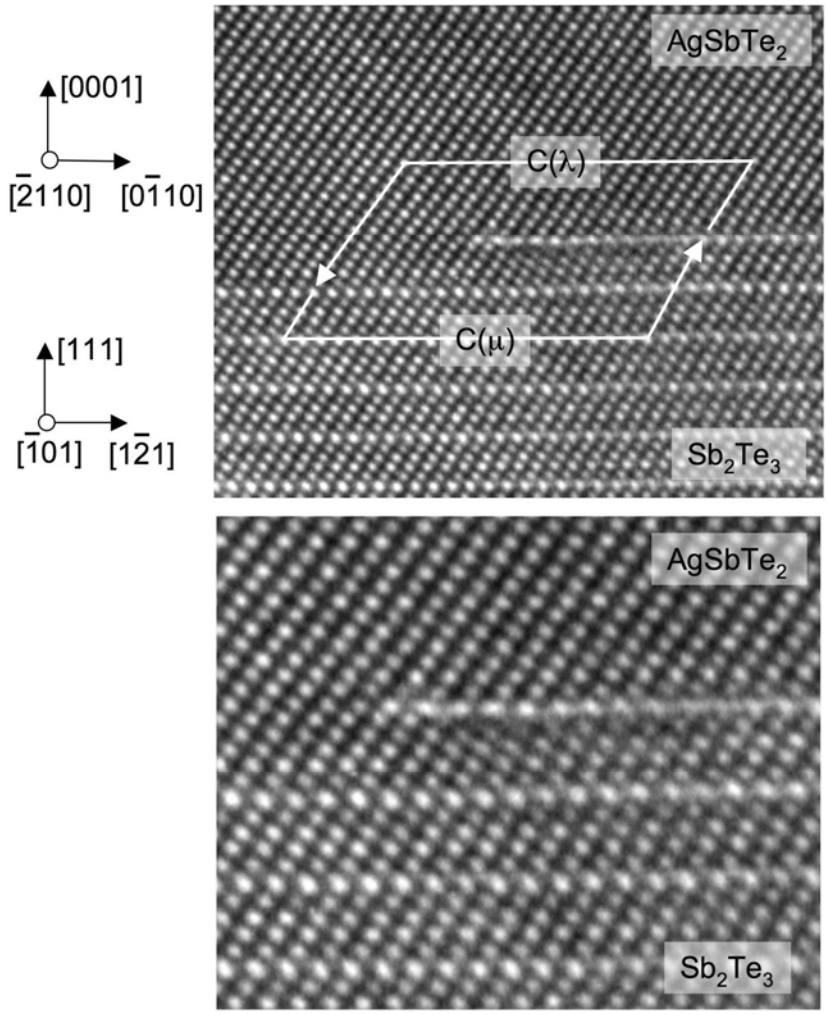

Figure 2.7. HRTEM image of the step-defect, or "disconnection," analyzed in this section. The step joins 6 close-packed planes in the upper $AgSbTe_2$ (λ) crystal ($h_\lambda = \sqrt{3}a_{cub}$) crystal to 5 close-packed planes in the Sb_2Te_3 (μ) crystal ($h_\mu = c_{hex}/3$). From the circuit elements of $\mathbf{C}(\lambda) = \frac{1}{4}[-25, 38, -25] \pm \frac{1}{4}[-1,0,1]$ in the upper crystal and $\mathbf{C}(\mu) = \frac{1}{6}[-65, -130, 2] \pm \frac{1}{2}[1,0,0]$ in the lower crystal, application of equation 2.6 gives a Burgers vector of

$\mathbf{b} = \left(\frac{5}{6}a_{cub} - \frac{c_{hex}}{3\sqrt{3}},\ \frac{8}{6}a_{cub} - \frac{c_{hex}}{3\sqrt{3}},\ \frac{5}{6}a_{cub} - \frac{c_{hex}}{3\sqrt{3}}\right)$ (expressed in the rocksalt coordinate frame).

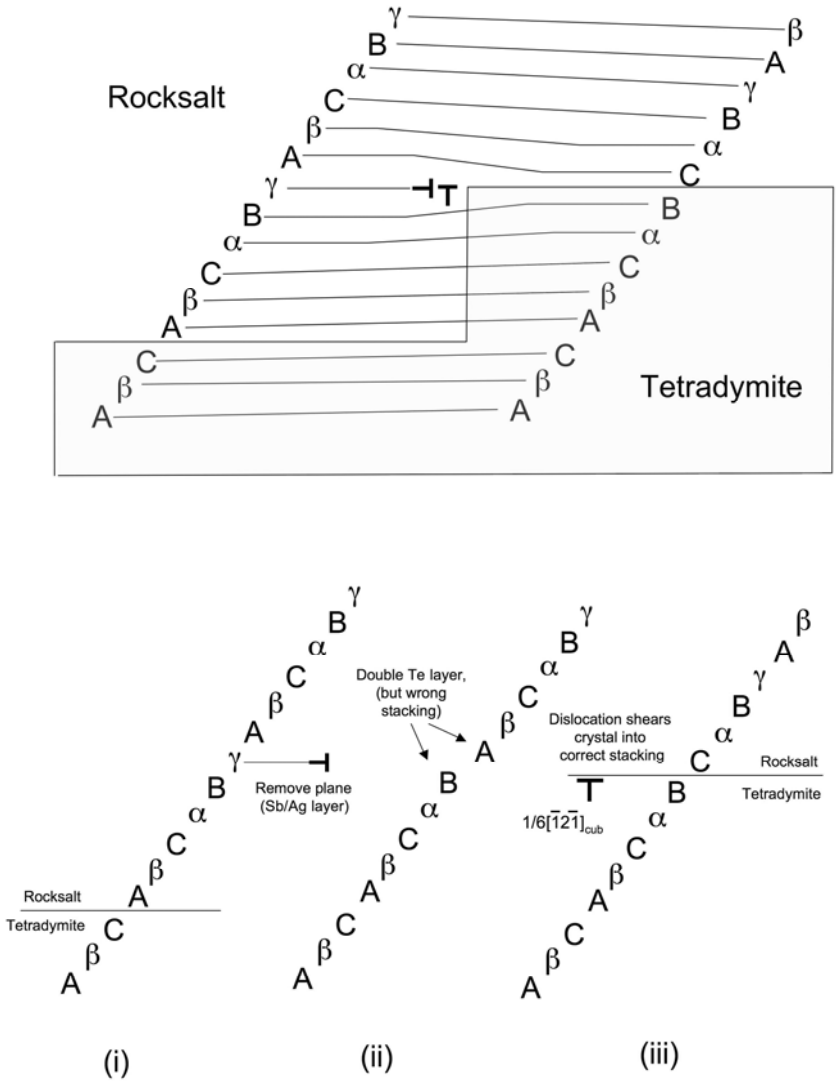

Figure 2.8. (a) Schematic of the observed interfacial disconnection. (b) Sequence of rearrangements produced by motion of the perpendicular and parallel components of the defect. Removal of the metal plane (g) in (i) by climb of the dislocation component normal to the interface, $\mathbf{b}_{\perp}$, produces two adjacent layers of Te in (ii), but leaves these layers in the wrong stacking sequence, BA. Glide of the parallel component, $\mathbf{b}_{\parallel}$, between these layers shears the crystal into the correct stacking, BC, thereby moving the rock-salt/tetradymite interface up to this plane.

3. Influence of Nanostructuring and Heterogeneous Nucleation on *zT* in $AgSbTe_2$

3.1 Introduction

As discussed in the previous section, solid-state precipitation provides one route to form and control nanoscale inclusions within a bulk material. In this section, we investigate how nanoscale solid-state precipitation systematically affects *zT* in a bulk thermoelectric material. Sb_2Te_3 precipitates were embedded within Sb-rich $AgSbTe_2$. In this system, we could vary precipitate size from nanometers to microns while tracking ρ, *S*, and κ. The transport data tracked the nucleation/growth and coarsening regimes of precipitation, separately determined from electron and optical microscopy. By thinking of this system as an $AgSbTe_2/Sb_2Te_3$ composite, we found that thermoelectric properties could be understood using effective medium theory simulations. Effective medium theory relates the transport properties of a macroscopically heterogeneous composite to that of its components (see e.g., ref.[36]). It was shown that the *zT* of a two component composite can never be larger than that of its constituents[37]. The effective medium behavior found in the $Sb_2Te_3/AgSbTe_2$ system therefore shows that precipitates do not increase *zT* in this case. Using microstructural measurements, we discovered that precipitates almost entirely nucleated at planar defects in the matrix and at grain boundaries. This heterogeneous nucleation caused precipitates to form a complex, interconnected network. We will argue that this is one reason our data is consistent with effective medium theory. One of the main conclusions of this work is that achieving *zT* improvement from nanostructuring through solid-state precipitation will require avoiding heterogeneous nucleation because this promotes effective medium behavior in transport properties.

3.2 Experimental Procedures

3.2.1 Sample Preparation

Our goal was to control second phase nucleation and growth of Sb_2Te_3 in the homogeneous $AgSbTe_2$ matrix. The alloy "$AgSbTe_2$" forms within the Ag_2Te-Sb_2Te_3 pseudobinary phase diagram. We found that the two most reliable phase diagrams are those reported by Maier *et al.[13]* and Marin *et al.[19]*. The positive slope of the Sb-rich $AgSbTe_2$ solvus boundary (Fig. 3.1) with Sb content allows one to tune precipitation by annealing at lower temperatures. In this system, the relevant precipitate is (Ag-doped) Sb_2Te_3 and the matrix is Sb-enriched $AgSbTe_2$, denoted henceforth as (Ag,Sb)Te. Having fixed the Sb content in this study, the equilibrium precipitate volume fraction depends on annealing temperature, as does the time scale for precipitation kinetics. We use the notation A:B to denote precipitate A forming in matrix B: $(Sb,Ag)_2Te_3$:(Ag,Sb)Te.

A homogeneous sample was synthesized at the stoichiometry of $Ag_{16.7}Sb_{30}Te_{53}$. The elements (~50 g total, 99.999 % purity) were melted together at 850 °C in a sealed

and evacuated quartz tube, followed by quenching to room temperature in ice water. This quenching step was critical for minimizing Ag_2Te precipitate formation. The sample was then annealed in the single phase δ region for 120 hours at 552 °C (Fig. 3.1, inset) and then quenched in ice water. The final ingot was about 1 cm in diameter and 3 cm long. This δ phase displayed a simple rocksalt X-ray powder diffraction pattern. No Sb_2Te_3 precipitates were observed either with X-ray diffraction or electron microscopy in these samples.

3.2.2 Microscopy and Transport Measurements

Microstructure was analyzed using TEM, SEM, and optical microscopy. Samples were polished and viewed in an optical microscope and SEM for coarse scale observation and electron micro probe analysis (EMPA). Electron transparent samples for the TEM were made by core drilling 3-mm thick discs followed by mechanical dimpling and ion milling. Conventional imaging and diffraction experiments were performed in a JEOL 2010F equipped with an Oxford EDS system and Gatan GIF for chemical analysis. In order to accurately measure the width of precipitates, electron diffraction was used to orient precipitates edge-on to their habit planes. Powder X-ray diffraction was performed on all samples.

The properties ρ, S, and κ were measured simultaneously on bar shaped samples using the Thermal Transport Option in a Quantum Design PPMS. For all pieces measured, approximately the same geometry (~2 mm^2× 6 mm) was used in order to further reduce systematic errors (e.g. due to geometry and thermal radiation). Four nickel contacts were electroplated onto the samples after polishing. Silver epoxy was then used to make Ohmic contacts to electrical leads, resulting in good (<1 Ω) 2-probe resistances. Hall effect measurements were performed using the Van der Pauw method and the AC Transport bridge of the Quantum Design PPMS up to ± 80 kOe magnetic field (H). Separate pieces were cut from the ingot into square shapes (~2×2 mm^2), then thinned to ~100 μm. Nickel contacts followed by silver epoxy were used for 1 mil Au wire electrical connections (<1 Ω) at the side corners. A 1 mA excitation current was used and no heating effects were observed.

3.2.3 Link between precipitation and transport measurements

In order to induce second phase precipitates at various stages of annealing, five pieces were cut from the starting homogeneous ingot at random and then separately annealed at 500 °C (heated at 15 °C/min) for 5, 15, 30, 60, and 120 minutes (Fig. 3.1, inset). All samples were quenched in iced water after annealing. We expected a precipitation reaction of the form $\delta \rightarrow \delta' + (Sb_{1-x}Ag_x)_2Te_3$ Judging from the phase diagram and EDS, the difference between δ and δ' was less than 1% Sb content, while x, the amount of Ag in Sb_2Te_3 precipitates was <5%. At this annealing temperature and Sb content, we estimated the equilibrium volume fraction at ~5-8% using the lever rule and area fraction measurements using optical micrographs of samples annealed for 4 hours. Precipitate size typically reached several μm after more than 2 hours of annealing at 500

°C. All samples had a grain size of ~1-2 mm, which stayed fixed during the precipitation annealing experiments. No change in oxide content was found for annealed samples.

In order to link changes in zT with the formation of precipitates, we compared microscopy and transport measurements on ingot pieces before and after annealing. We first measured transport on seven pieces (with similar geometry) of the ingot before annealing, yielding a measurement of the "homogenous" ingot. The transport values of the homogeneous ingot at room temperature were: ρ=6.5±0.7 mΩ cm, S=194±7 μV/K, κ=0.65±0.05 W/Km, carrier concentration $n=4\pm1\times10^{20}\text{cm}^{-3}$, yielding a zT=0.26±0.04. Since the microstructure was consistent throughout the ingot, a small variation in the carrier concentration likely caused the variation in the transport properties. We performed ρ, S, and κ measurements on the five aforementioned annealed pieces and compared their properties to adjacent un-annealed pieces to partly control for carrier concentration variations. Three annealed pieces were measured this way for Hall effect measurements.

The geometrical errors in ρ and κ measurements led to a nearly 50 % uncertainty in the absolute value of zT, so we focused on ρ, S, κ, and n individually and considered the largest source of error (either ingot variation or geometry). There was no change in the homogeneous sample properties with time (below 400 K) over the course of the annealing experiments.

3.3 Results

3.3.1. Thermoelectric Transport and Effective Medium Behavior

The transport properties of the matrix δ phase are consistent with homogeneous Sb-rich $AgSbTe_2$ (representative sample, Fig. 2). S and ρ monotonically increased with increasing T. κ was weakly T-dependent with a low magnitude, consistent with previous reports[38]. The Hall number (R_H) was positive (in agreement with the sign of S) and weakly T-dependent. We found that samples with different signs for R_H and S were contaminated with minute amounts of Ag_2Te as reported for $AgSbTe_2$ earlier[24, 39] and were discarded from this study. The Hall resistivity (ρ_{Hall}) was linear in H for the entire T-regime studied, justifying the simple relation[i] $n=1/eR_H$, where e is the electron charge. The carrier concentration for this particular sample was $\sim2.6\times10^{20}\text{cm}^{-3}$ at 300 K. From the transport data, our starting ingot $Ag_{16.7}Sb_{30}Te_{53}$ was a degenerate semiconductor with p-type charge carriers.

As a function of annealing time, ρ decreased and κ increased (Fig. 3.3). For clarity, only 300 and 400 K measurements are shown. The dashed regions in Fig. 3.3 indicate the variation (one standard deviation) of the pre-annealed ingot properties. $\Delta\rho$ (and $\Delta\kappa$, Δn, ΔS) is defined as the difference $\rho(t) - \rho(0)$. Here t is the annealing time, $\rho(0)$ was measured on an un-annealed piece, and $\rho(t)$ was measured on a separate piece, adjacent to that used for $\rho(0)$, after annealing. At t>30 minutes, $\Delta\rho$ decreases with time (Fig. 3.3a). At t<30 minutes, $\Delta\rho$ does not vary monotonically. This short annealing time behavior was not reproducible on separate trials and so probably resulted from cracks introduced during rapid heating/cooling cycles. An increase in κ is also visible after annealing for 120 minutes (Fig. 3.3b). The variation in $\Delta\kappa$ roughly tracks that of $\Delta\rho$, as

determined by the Weidemann Franz law (black dots, Fig. 3.3b). The large error bars in the ρ and κ data sets are due to geometry. The concentration n (=1/eR_H) decreased with annealing time (Fig. 3.3b, inset) consistent with the behavior $\Delta\rho$ and a constant carrier mobility.

ΔS had a much clearer change in t, even at early times, and could be closely compared with the introduction of precipitates determined through X-ray powder diffraction (Fig. 3.4). The powder diffraction data provided bulk-averaged, semi-quantitative measurements of precipitate formation. The intensity of the highest visible Sb_2Te_3 X-ray peak, the (1 0 10) plane (Fig. 3.4a, inset), increased monotonically as a function of t (Fig. 3.4a). Assuming the main contributor to the intensity change is precipitate volume fraction, Fig. 3.4a signals an increasing precipitate volume fraction with annealing time consistent with the expected precipitate reaction. The X-ray intensity t-dependence has two different regimes: intensity increased sharply for t<30 minutes and became nearly constant for t>30 minutes. ΔS (Fig. 3.4b) also changed with annealing at two different time scales (Since S involves no geometrical measurements the error bars were much less than in ρ and κ, and were taken from the ingot variation (dashed region in Fig. 3.4b). Using similarly shaped samples also reduced systematic errors from the absolute geometry). For t<30 minutes, ΔS decreased more rapidly than for t>30 minutes. In the entire t-regime, ΔS was always bounded by that of (Ag,Sb)Te (dashed region) and pure $(Sb,Ag)_2Te_3$ (shaded region). This ΔS cannot be explained only through the behavior of Δn (Fig. 3b, inset) since S normally increases with decreasing n in degenerate semiconductors[7]. However, the common t-dependence of ΔS and X-ray intensity suggests a link between the transport properties and precipitate volume fraction.

The t-dependence of the transport data suggests an analysis based on the effective medium theory of composites. First, Fig. 3.4 shows that there is an explicit link between transport and volume fraction. Second, $\Delta S(t)$ (Fig. 3.4b) is sharply bounded by the separate properties of precipitate and matrix, in agreement with strict bounds derived from analytical effective medium theory[37]. Note that both $(Sb,Ag)_2Te_3$ and (Ag,Sb)Te are p-type.

Consider a composite made up of only two components (A, B). A general expression for the effective (E) composite (thermal and electrical) conductivity as a function of volume fraction has been proposed by McLachlan *et al.[40]*:

$$x_A \frac{\sigma_A^{1/\tau} - \sigma_E^{1/\tau}}{\sigma_A^{1/\tau} + a\sigma_E^{1/\tau}} = (1 - x_A)\frac{\sigma_E^{1/\tau} - \sigma_B^{1/\tau}}{\sigma_B^{1/\tau} + a\sigma_E^{1/\tau}} . \qquad (3.1)$$

Here, x_A is the volume fraction of component A and σ is the electrical (or thermal) conductivity of A, B, or E. The constant a=(1-x_C)/x_C, where x_C is the "percolation threshold". In the present context, x_C would correspond to the critical x_A at which precipitates become interconnected. When σ_A/σ_B <<1, τ is the scaling exponent of σ_E near the percolation threshold. When $\sigma_A \sim \sigma_B$ (as in the present case), McLachlan *et al.* suggested that τ will depend on microstructure[40]. Bergman *et al.* extended the effective medium theory to describe the thermopower as[41]:

$$S_E = S_B + (S_A - S_B)\frac{(\kappa_E/\sigma_E)(\sigma_B/\kappa_B)-1}{(\kappa_A/\sigma_A)(\sigma_B/\kappa_B)-1}. \quad (3.2)$$

In equation 3.2, κ_E and σ_E are computed using equation (3.1). These equations were used successfully describe the transport properties of alloys with second phase precipitates at large volume fractions[42].

Using equations 3.1 and 3.2, we simulated the effective medium theory prediction by letting A=$(Sb,Ag)_2Te_3$ and B=(Ag,Sb)Te and then using the data of Lostak *et al.[43]* and Fig. 3.2, respectively. In order to compare the simulations with the data, the absolute volume fraction had to be estimated. First, the equilibrium volume fraction was measured (~7.2 %, consistent with the lever rule) by determining the precipitate area fraction from several optical micrographs of samples annealed for more than 4 hours (where precipitates became more than 1 μm in size). The *t* dependence of the X-ray intensity (Fig. 3.4a) was then normalized by assuming that samples annealed at 2 hours or more had the equilibrium precipitate volume fraction.

The parameters τ and x_C were varied and compared to the $\Delta\rho$, $\Delta\kappa$, and ΔS data (Fig. 3.5a, b, and c, respectively). Even assuming 3D percolation in a random, continuous medium, the value of x_C and τ will greatly depend on the geometry of precipitates. We compared four different curves: (1) x_C=0.15, which was the lowest[44] value found in the literature for the 3D continuum threshold with spheres, with τ=1 (red line), (2) parallel conduction (dashed line), (3) x_C=0.03, with τ=1 (blue line), and (4) x_C=0.03 and τ=2 (brown line, ΔS plot only). (For parallel conduction, the electrical/thermal conductivity is given by $\sigma_E = x_A\sigma_A + (1-x_A)\sigma_B$ and $S_E = (x_A\sigma_A S_A + (1-x_A)\sigma_B S_B)/(x_A\sigma_A + (1-x_A)\sigma_B)$.) Another uncertainty in the simulation will come from how well the properties of the components are known. The spread in properties reported for $(Sb,Ag)_2Te_3$ [43]will produce a spread in the simulations, as shown around the x_C=0.03/τ=1 and x_C=0.15/τ=1 ΔS curves (Fig. 3.5c) only for clarity. The simulations reveal that our transport data is consistent with the effective medium theory within the uncertainties of the measurements and known properties of $(Sb,Ag)_2Te_3$ and (Ag,Sb)Te. In order to interpret the approximate range of parameters (e.g. x_C~0.03 and τ=1), further knowledge of the microstructure is needed.

3.3.2 Precipitate Microstructure and Heterogeneous Nucleation

Although the δ phase has a simple rocksalt structure, we found that its microstructure, is complex. We observed a dense array of interconnected planar defects, typically microns long. In Fig. 3.6a, a typical bright field image, viewed on the [110] zone axis, revealed a series of bands and sharp lines. By rotating the sample, we found that the bands and lines were a kind of planar defect inclined with respect to each other. These features were always observed to be interconnected. By comparing the bright field image with corresponding diffraction pattern (Fig. 6a, inset), the planar defects were found to be oriented along the close-packed planes of the host rocksalt structure, suggestive of a stacking fault. For example, when viewed on the [110] axis the defects are

edge on and appear bright, occurring along ($\bar{1}11$) and ($1\bar{1}1$) planes. Defects were always oriented at 110°, close to 109.5° expected between ($\bar{1}11$) and ($1\bar{1}1$) planes. Planar defects were always found oriented along one of the close packed (111) family of planes. When tilted away from a high-symmetry zone axis, these planar features had bright/dark fringe contrast typically seen in stacking faults. For clarity, we now tentatively refer to the observed planar defects as stacking faults. Coarse scale microscopy (optical, SEM) revealed only grain size structure, for which no preferred orientation, relative to the growth axis, was found.

Nucleation and growth of precipitates occurs during annealing times <30 minutes. Fig. 4.6b shows a typical bright field image ([110] zone axis) after 15 minutes of annealing. Precipitates were identified using selected area diffraction. With its larger repeat distances, Sb_2Te_3 tetradymite diffraction spots will be more closely spaced than that of rocksalt (Ag,Sb)Te. The diffraction pattern ([110] zone axis, inset Fig. 4.6b), shown for area 1 of Fig. 4.6b, is a superposition of the matrix rocksalt pattern and one in which 8 additional superlattice reflections occur parallel to the close packed ($1\bar{1}1$) rocksalt plane. The tetradymite structure should exhibit 5 extra superlattice reflections. The presence of extra superlattice reflections indicates that precipitates are a metastable Sb-Te phase. Samples annealed for t<30 minutes typically had these metastable Sb-Te phases. Nevertheless, precipitates were always found oriented along the rocksalt close packed planes and took the form of long (~μm), thin (~40 nm) plates. Stacking faults (area 2 of Fig. 6b) were also observed in the surrounding rocksalt matrix, identical to those found in Fig. 6a. This similarity in orientation relationship and aspect ratio suggests that stacking faults serve as heterogeneous nucleation sites for precipitates.

For *t*>30 minutes of annealing, larger precipitates began to appear with the Sb_2Te_3 tetradymite structure, consistent with the precipitate reaction expected from the phase diagram. Fig. 4.6c shows a typical bright field image ([110] zone axis) of a sample annealed for 120 minutes. The diffraction pattern (inset, Fig. 4.6c) shows a superposition of the rocksalt and tetradymite patterns, notably with 5 extra superlattice reflections. These Sb_2Te_3 precipitates were about a micron wide. The superlattice reflections were parallel to the close packed ($1\bar{1}1$) rocksalt plane. In the tetradymite structure, the observed superlattice reflections (Fig. 4.6c, inset) are parallel to the (0001) family of planes. This implies that Sb_2Te_3 and (Ag,Sb)Te were oriented such that their close packed planes containing Te atoms lined up. Precipitate formation observed here was very similar to the isomorphic PbTe-Sb_2Te_3 system[29]. Samples annealed longer than 120 minutes produced no significant changes in precipitate size, morphology, or composition.

For samples annealed more than 2 hours, precipitates, being a micron or more in size, could be viewed using optical microscopy. In Fig. 4.6d, a typical optical micrograph is shown. The white regions correspond to precipitates. These precipitates were confirmed to be $(Sb,Ag)_2Te_3$ using an SEM. The vast majority of micron-sized precipitates were found near grain boundaries. While some smaller precipitates were found within the grains, the large precipitates comprise most of the volume fraction. By extracting precipitate area fraction from these images, we found the precipitate volume fraction of ~7.3 %, within that expected from the lever rule, and used in the analysis of

Fig. 4.5. From Fig. 4.6d, we concluded that grain boundaries, in addition to the stacking faults found in the matrix phase, provide heterogeneous nucleation centers for precipitates in this system.

The annealing time dependence of the microstructure agreed qualitatively with the time dependence of the transport properties (Fig. 4.3 and 4.4) and the bulk averaged X-ray diffraction (Fig. 4.4). In particular, the presence of many small precipitates for $t<30$ minutes (Fig. 4.6b) suggests that nucleation and growth occurs in this annealing regime. For $t>30$ minutes, significantly larger precipitates were observed with fewer nanoprecipitates, suggestive of coarsening behavior. This separation of time scales qualitatively matches the previous bulk measurements. However, the detailed microstructure was very complicated. Precipitates in $(Sb,Ag)_2Te_3$:(Ag,Sb)Te were highly anisotropic, long and plate-like, and did not nucleate homogenously throughout the sample. We found that heterogeneous precipitate nucleation will result from (1) the preexisting planar defects (likely stacking faults) in the (Ag,Sb)Te matrix and (2) grain boundaries. At early stages of precipitation, surprisingly, a metastable Sb-Te phase formed rather than Sb_2Te_3, expected from the phase diagram. At longer annealing times, the precipitates had the equilibrium Sb_2Te_3 structure. Though the metastable phase found at early annealing times complicates the fine details of the effective medium analysis (section IIb, Fig. 5), we can conclude that heterogeneous nucleation will force the percolation threshold, x_C, to a very small, if not zero value. This will be true even ignoring the spherical precipitate continuum approximation of Fig. 4.5. In the limit of $x_C \rightarrow 0$ and $t \rightarrow 1$, the generalized effective medium equations reduce to purely parallel conduction[42]. The simulations of Fig. 4.5 therefore suggest that the data is close to a parallel conduction model, since agreement between simulation/data becomes poorer by increasing either x_C or τ.

3.4 Discussion and Conclusions

A binary composite effective medium theory provides the most consistent explanation for the change in the transport data with annealing time observed in our experiments. Furthermore, the simulations in Fig. 4.5 point to a composite microstructure favoring parallel conduction. Microstructural observations support the conclusions of the effective medium simulations because precipitates are always found in an interconnected network. This observation holds at very small scales, where nanoprecipitates nucleate at interconnected stacking faults, and at larger scales, where micron size precipitates decorated grain boundaries.

Both grain boundaries and stacking faults seem to serve as preferred nucleation sites for precipitates, and therefore promote heterogeneous nucleation. Solid-state precipitation involves an activation barrier for nucleation that is significantly reduced at imperfections such as a grain boundary (e.g. [45]). Sb_2Te_3 precipitation at planar defects in the (Ag,Sb)Te matrix is also a form of heterogeneous nucleation.

Avoiding a non-uniform, interconnected network due to heterogeneous nucleation poses a significant hurdle to realizing zT gains through nanostructuring by solid-state

precipitation. On the basis of an analytical effective medium theory, Bergman *et al.* established strict bounds on thermoelectric properties of a two component composite[37]. Assuming the analytic theory holds, a thermoelectric composite will obey the inequality: $z_E T < \mathrm{Max}(z_A T, z_B T)$; the effective (E) zT will never be larger than that of its components (A, B). As noted previously, $\Delta S(t)$ (Fig. 3.4b) obeys the bounds for the analytic effective medium theory: $S_B < S_E < S_A$ (with $S_A > S_B$). These bounds do not depend on the detailed microstructure of the composite if the analytic theory holds. The analytic effective medium theory is strictly valid far from the percolation threshold. Heterogeneous nucleation promotes an interconnected network of precipitates. This pushes $x_C \rightarrow 0$ and therefore causes the precipitate/matrix system to be far from the percolation threshold at all finite volume fractions, guaranteeing the validity of the analytic effective medium theory and reduction of zT.

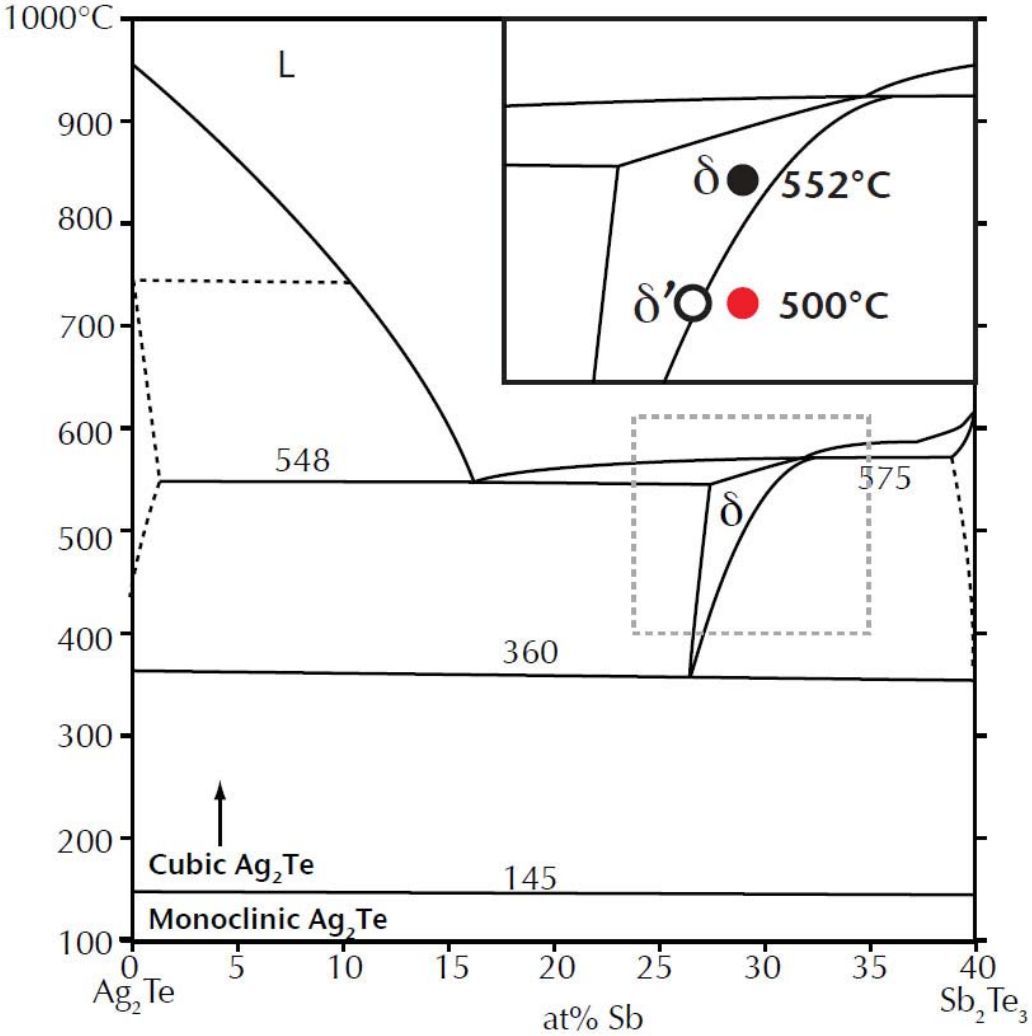

Figure 3.1 Synthesis and control of nanoprecipitates in thermoelectric alloy (Ag,Sb)Te. (a) The homogeneous $AgSbTe_2$ δ phase occurs in the Ag_2Te-Sb_2Te_3 pseudobinary system. Inset: Enlarged view of phase diagram in (a). A solid state precipitation reaction d-->d'+$(Sb,Ag)_2Te_3$ occurs at 500 °C, where the d phase (30 at.% Sb) decomposes into an Sb deficient (~29 at. %) d' phase with Ag-doped Sb_2Te_3 precipitates.

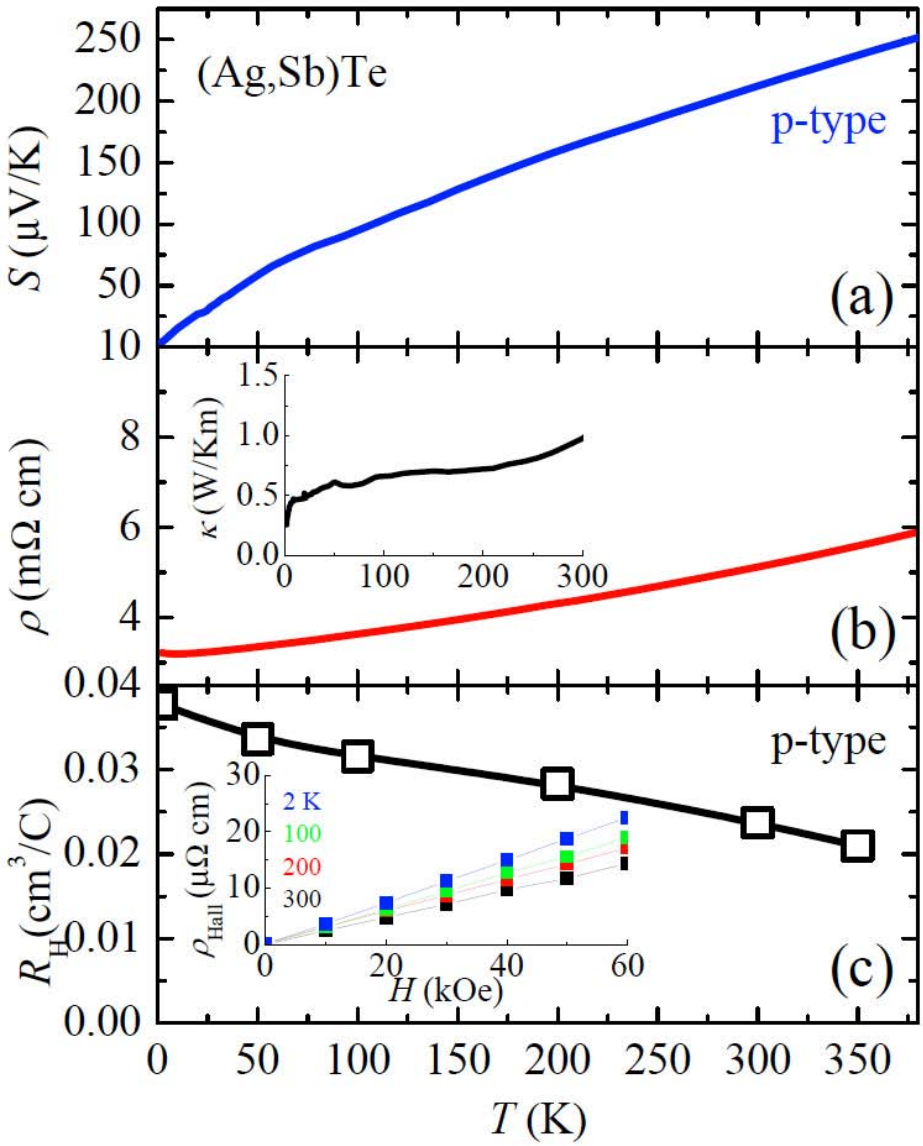

Figure 3.2 Representative transport properties of the homogeneous δ (a) Seebeck coefficient (*S*) versus temperature (*T*). All samples were p-type. (b) Resistivity (ρ) versus *T*. Inset: Thermal conductivity (κ) versus *T*. (c) Hall number (R_H) versus T. Inset: The Hall resistivity (ρ_{Hall}) was linear as a function of magnetic field (*H*). All samples were p-type, in agreement with *S*(*T*), in the entire *T*-regime studied.

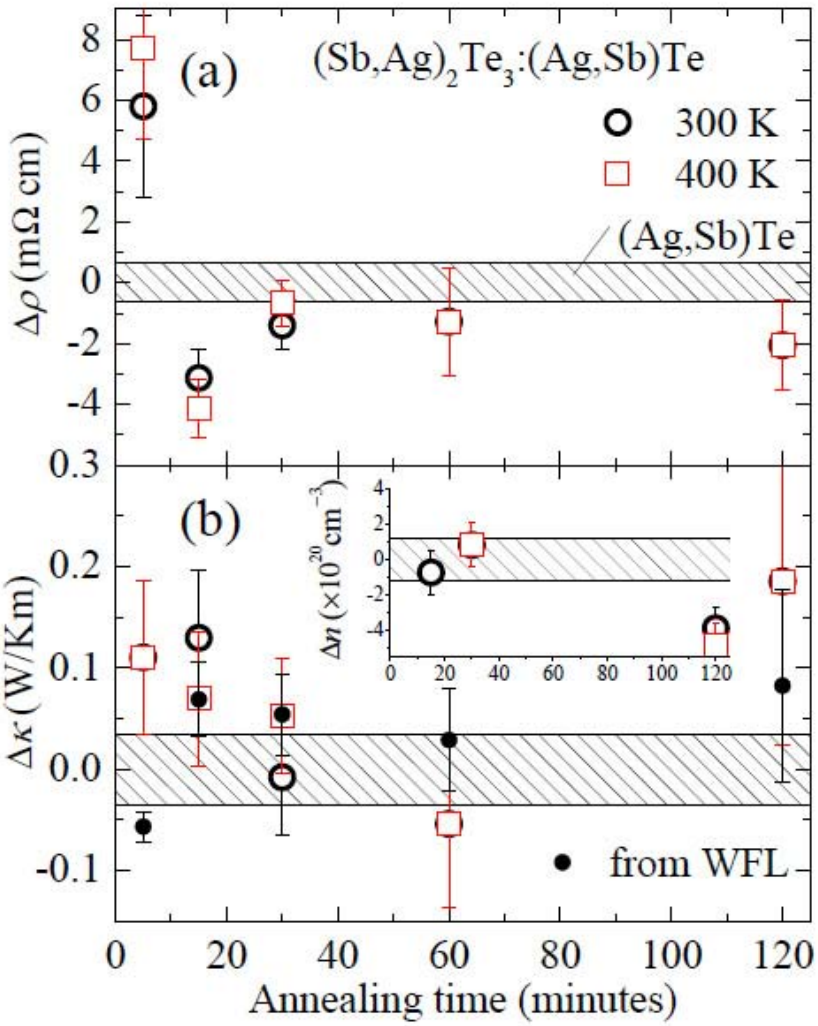

Figure 3.3 Change in average transport properties of homogeneous δ with the introduction of $(Sb,Ag)_2Te_3$ precipitates. The variation in properties across the homogeneous ingot is indicated by the dashed area. Error bars shown are the larger of the ingot variation or geometrical error. Measurements were taken at 300 K and 400 K. (a) The resistivity ($\Delta\rho$) did not significantly change versus annealing time.(b) Variations in the total thermal conductivity ($\Delta\kappa$, open circles) are partly explained by changes in ρ given by the Weidemann Franz law (WFL). No significant change is seen in $\Delta\kappa$ versus annealing time.

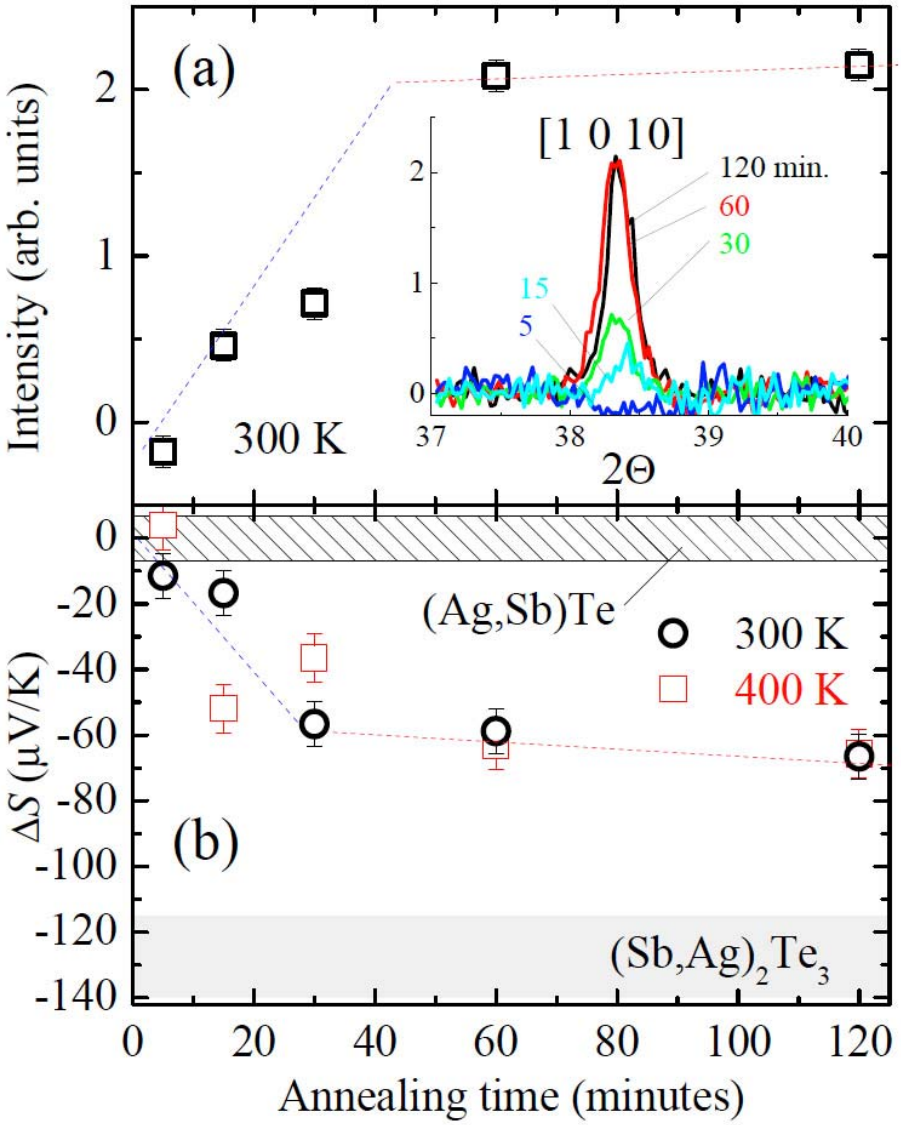

Figure 3.4 ΔS shares a common time dependence with the formation of Sb_2Te_3 precipitates as determined from powder X-ray diffraction. (a) Peak intensity of the [1 0 10] Sb_2Te_3 peak as a function of annealing time at 500 °C. Inset: Raw Xray intensity versus 2Θ of the peak displayed in (a) at different annealing times. (b) ΔS versus annealing time shares the same time dependence as the Xray data in (a). The shaded region corresponds to the expected difference in S between δ and p-type Ag-doped Sb_2Te_3. S for (Ag,Sb)Te with $(Sb,Ag,)_2Te_3$ precipitates is bounded by that for pure (Ag,Sb)Te and pure $(Sb,Ag)_2Te_3$.

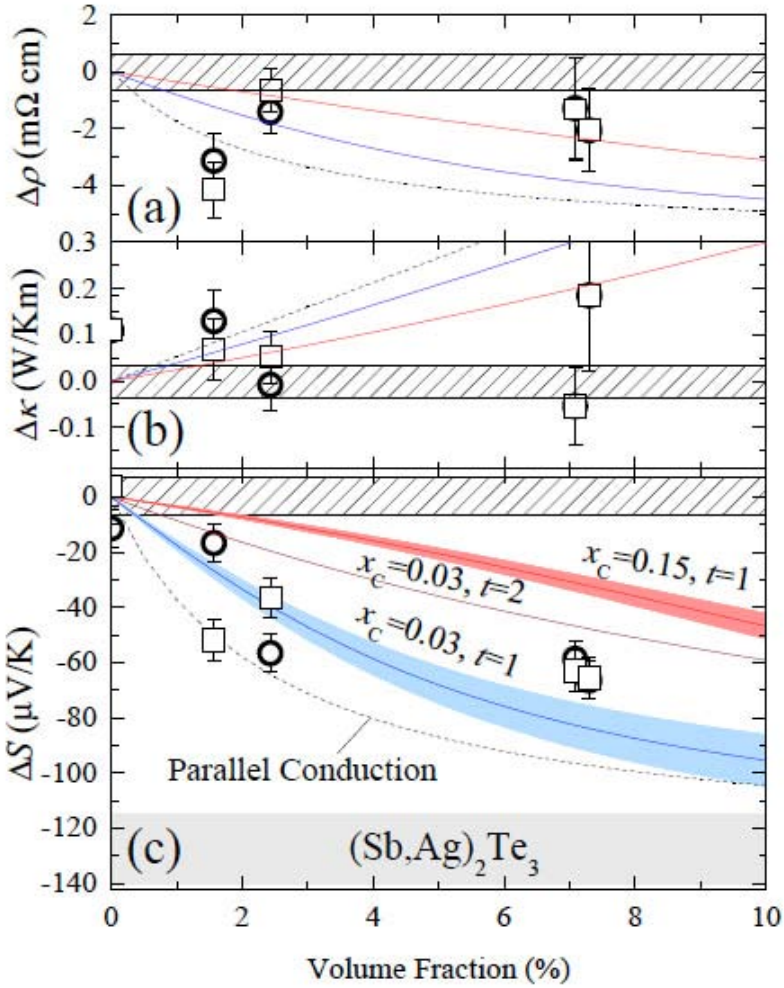

Figure 3.5 Transport properties compared with calculations from effective medium theory.

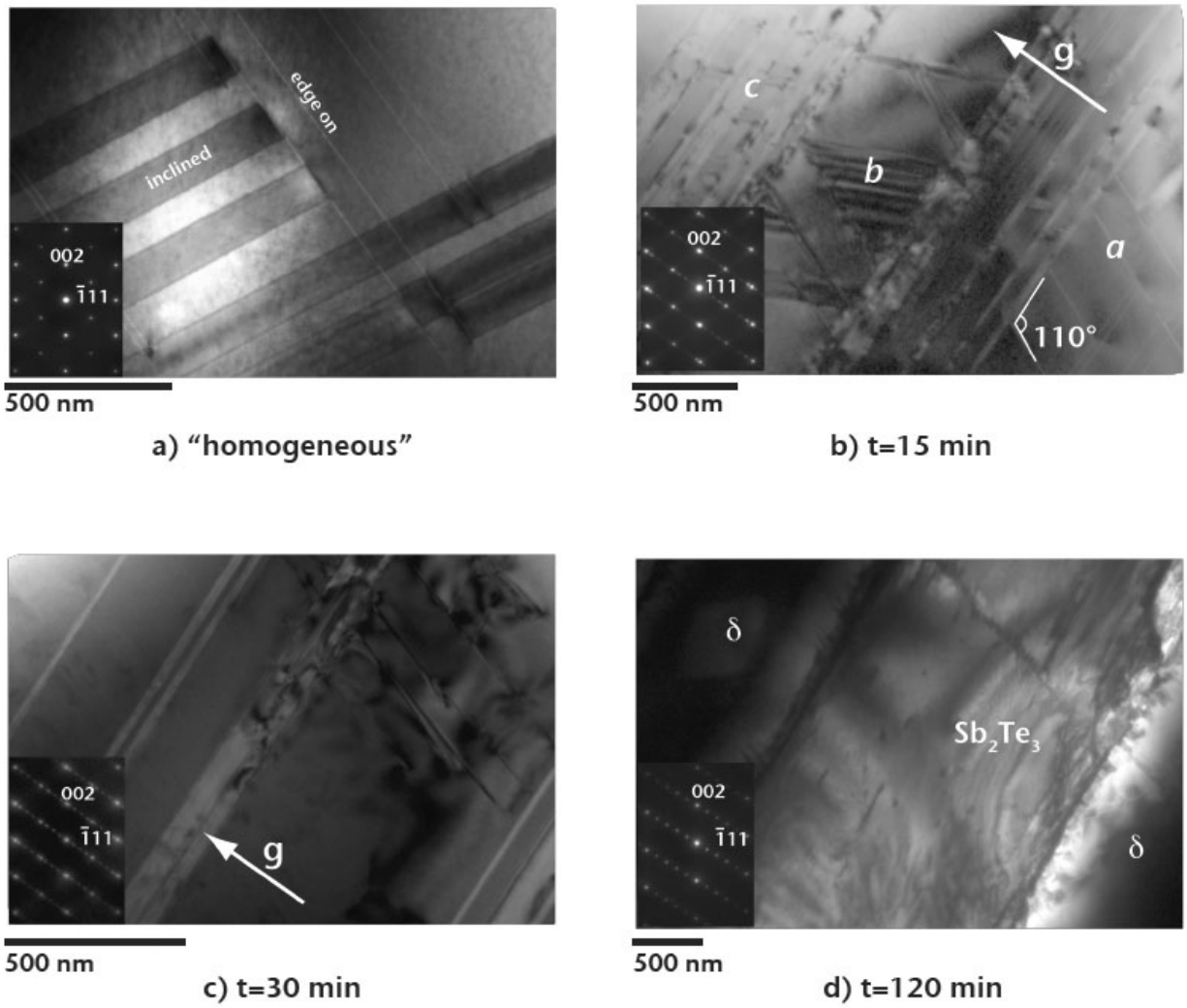

Figure 3.6 Representative microstructures observed by TEM as a function of time. Insets show electron diffraction patterns. (a) Initial microstructure of the "homogeneous" δ-phase contains large number of planar defects. (b), (c) initial precipitation occurs with metastable formation of tetradymite-type structure. (d) at long times, the equilibrium Sb_2Te_3 plates form.

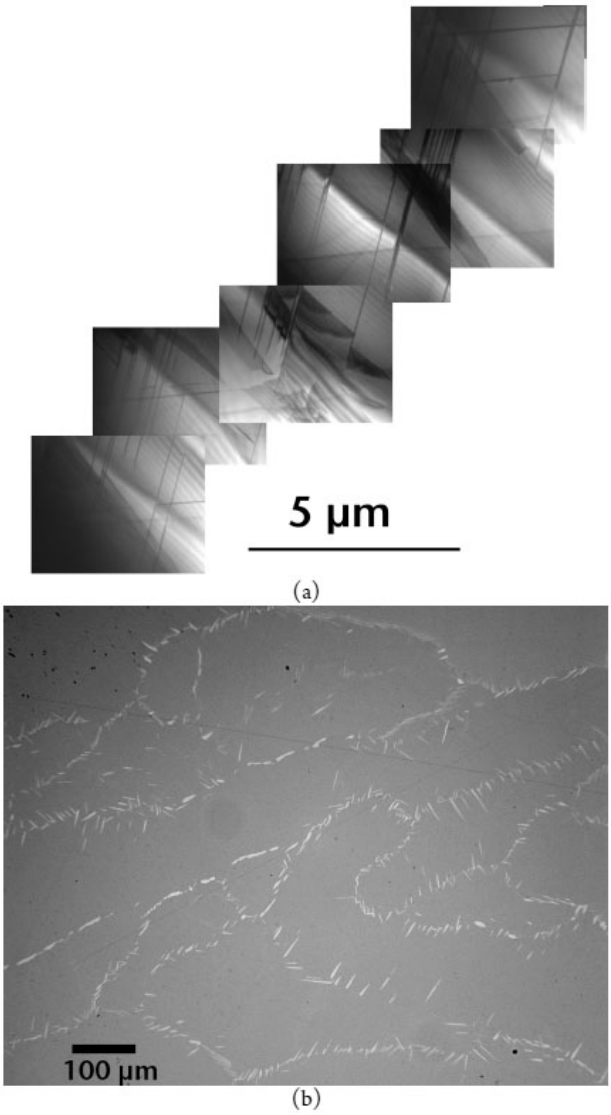

Figure 3.7 Precipitates form a percolating network (a) Composite BF TEM image showing many planar defects. Since planar defects form an interconnected network in the unannealed δ phase. Precipitates preferentially nucleate at planar defects upon annealing. (b) Optical bright field micrograph of sample annealed for 4 hours at 500 °C. Large mm size precipitates decorate grain boundaries. Grain boundaries are therefore also nucleation sites for Sb_2Te_3 precipitates in $AgSbTe_2$.

4. Theory of Thermoelectric Enhancement Due to Nanoinclusions

In this section, we present a theoretical model and numerical calculations of the thermoelectric properties of bulk semiconductors containing metallic nanoparticles [46]. Our model considers scattering of electrons on the band bending at the interfaces between the semiconductor host and randomly distributed metallic islands. This causes energy dependent scattering of electrons, leading to an energy filtering effect that increases the Seebeck coefficient. This provides an explicit physical model for the proposed energy filtering effect [3]. By combining this model with a model for phonon scattering on the nanoinclusions, we predict significant enhancement of the zT factor. We point out that while the role of metallic nanoinclusions may appear at first to be similar to that of point defects for which extensive work has been done, the physics is actually quite different. Indeed, in addition to the electronic scattering, the phonon scattering on nanoinclusions occurs in a completely different regime than that on point defects, as will be discussed in Sec. IV B. The central idea in this paper is illustrated in Fig. 4.1. There, spherical metallic nanoinclusions with radius R and volume fraction x are randomly distributed in a bulk semiconductor material. In general, at such metal/semiconductor interfaces, charge transfer between the metal and the semiconductor leads to band bending away from the interface, characterized by the electrostatic potential $V(r)$ (Fig. 4.1b). The presence of this potential causes *energy-dependent* scattering of electrons, as illustrated in Fig. 4.1c. The high energy electrons are unaffected by the potential, but the low energy electrons can be strongly scattered. Because the Seebeck coefficient depends on the energy derivative of the relaxation time $d \ln \tau(E)/dE$ at the Fermi energy, this type of energy filtering is precisely the prescription to increase the Seebeck coefficient of thermoelectric materials.

Our theoretical model is based on the Boltzmann transport equation (BTE) within the relaxation time approximation. We apply the model to a system of *n*-doped PbTe with metallic nanoinclusions because of the availability of experimental data and good understanding of scattering mechanisms in bulk PbTe [47-49], although the theory can be used for any thermoelectric material.

4.1 CHARGE AND HEAT TRANSPORT IN BULK PbTe

In this section we will review the expressions[47-49] for the charge and heat transport in bulk PbTe with *n*-type doping. The valence band of PbTe contains four energy minima located at the L points. The energy dispersion relation near each minimum is usually described by the Kane model[47]

$$\frac{\hbar^2 k_l^2}{2m_l^*} + \frac{\hbar^2 k_t^2}{m_t^*} = E(1 + E/E_g) \tag{4.1}$$

where E_g is the direct energy gap of PbTe, $\hbar$ is the Planck constant, and k and m^* are the electron wave vector and effective mass (at minimum energy point k=0, E=0) along the longitudinal (suffix l) and transverse (suffix t) directions of the corresponding L point. For n-type PbTe, the electron concentration is given by

$$n[E_F] = \frac{(2m_d^* k_B T)^{3/2}}{3\pi^2\hbar^3}\int_0^\infty \gamma(z)^{3/2}\left(-\frac{\partial f_0}{\partial z}\right)dz \tag{4.2}$$

where $m_d^* = 4^{2/3}(m_l^* m_t^{*2})^{1/3}$ is the density of states effective mass in which the fourfold degeneracy is included, k_B is the Boltzmann constant, and $f_0(z)$ is the Fermi function written in terms of dimensionless variables $z=E/(k_BT)$ and $z_F=E_F/(k_BT)$. E_F is the Fermi energy and the function $\gamma(z)=z+bz^2$, where $b=k_BT/E_g$. In the relaxation time approximation the BTE expressions for electrical conductivity, σ, Seebeck coefficient, S, and electron contribution to thermal conductivity, κ_e, are[47]

$$\sigma = \frac{e^2}{m_c^*}\frac{(2m_d^* k_B T)^{3/2}}{3\pi^2\hbar^3}\langle\tau(z)\rangle, \tag{4.3}$$

$$S = \frac{k_B}{e}\frac{\langle\tau(z)(z-z_F)\rangle}{\langle\tau(z)\rangle}, \tag{4.4}$$

and

$$\kappa_e = \sigma T\frac{k_B^2}{e^2}\left\{\frac{\langle\tau(z)z^2\rangle}{\langle\tau(z)\rangle} - \left[\frac{\langle\tau(z)z\rangle}{\langle\tau(z)\rangle}\right]^2\right\}, \tag{4.5}$$

where $m_c^* = 3/(1/m_l^* + 2/m_t^*)$ is the effective conductivity mass, and the average is defined as:

$$\langle A(z)\rangle \equiv \int_0^\infty \frac{\gamma(z)^{3/2}}{1+2bz}\left(-\frac{\partial f_0}{\partial z}\right)A(z)dz. \tag{4.6}$$

In bulk PbTe at room temperature the dominant contributions to the total relaxation time, $\tau_{\text{bulk}}(z)$, are scattering by the deformation potential of acoustic and optical phonons, and polar scattering by optical phonons [47-49]. We also take into account scattering on the short-range potential of vacancies although it gives a much smaller contribution compared to scattering by phonons. Thus, the total relaxation time for bulk PbTe is given by:

$$\frac{1}{\tau_{\text{bulk}}(z)} = \frac{1}{\tau_{\text{PO}}(z)} + \frac{1}{\tau_a(z)} + \frac{1}{\tau_o(z)} + \frac{1}{\tau_v(z)}. \tag{4.7}$$

The relaxation time due to polar scattering by optical phonons reads [47, 49]

$$\tau_{\text{PO}}(z) = \frac{\hbar^2 \gamma(z)^{1/2} F^{-1}}{e^2 (2m_{d1}^* k_B T)^{1/2} (\epsilon_\infty^{-1} - \epsilon_0^{-1}) \gamma'(z)}, \tag{4.8}$$

where $m_{d1}^* = (m_l^* m_t^{*2})^{2/3}$ is the density of states effective mass in the single valley, the function $\gamma'(z)=1+2bz$, and ε_0 and ε_∞ are the static and high frequency permittivities, and

$$F = 1 - \delta \ln\left(1 + \frac{1}{\delta}\right) - \frac{2bz(1+bz)}{(1+2bz)^2} \times \left[1 - 2\delta + 2\delta^2 \ln\left(1 + \frac{1}{\delta}\right)\right]. \tag{4.9}$$

Here $\delta = (2kr0)^{-2}$ with r_0 the screening length of optical phonons:

$$r_0^{-2} = \frac{2^{5/2} e^2 m_d^{*3/2} (k_B T)^{1/2}}{3\pi^2 \hbar^3} \int_0^\infty \gamma(z)^{1/2} \gamma'(z) \left(-\frac{\partial f_0}{\partial z}\right) dz. \tag{4.10}$$

The relaxation time due to scattering by the deformation potential of acoustic and optical phonons, and also due to scattering on the short range potential of vacancies can be written generally as [47, 49],

$$\tau_m(z) = \frac{\tau_{0,m}}{\gamma(z)^{1/2} \gamma'(z) [(1-A)^2 - B]}, \tag{4.11}$$

where $A=bz(1-K_m)/\gamma'(z)$, and $B=8bz(1+bz)K_m/(3\gamma'^2(z))$, with the suffix $m=a$ for acoustic phonons, $m=o$ for optical phonons, and $m=v$ for vacancies. The constants $\tau_{0,m}$ and K_m are defined as

$$\tau_{0,a} = \frac{2\pi\hbar^4 C_l}{E_{ac}^2 (2m_{d1}^* k_B T)^{3/2}}, \quad K_a = \frac{E_{av}}{E_{ac}}, \tag{4.12}$$

$$\tau_{0,o} = \frac{2\hbar^2 a^2 (\hbar\omega_0)^2 \rho}{\pi E_{oc}^2 (2m_{d1}^* k_B T)^{3/2}}, \quad K_o = \frac{E_{ov}}{E_{oc}}, \tag{4.13}$$

$$\tau_{0,v} = \frac{\pi\hbar^4}{U_{vc}^2 m_{d1}^* (2m_{d1}^* k_B T)^{1/2} N_v}, \quad K_v = \frac{U_{vv}}{U_{vc}}. \tag{4.14}$$

Here C_l is a combination of elastic constants, E_{ac} and E_{av} are the acoustic phonon deformation potential coupling constants for conduction and valence bands, E_{oc} and E_{ov} are optical phonon deformation potential coupling constants for conduction and valence bands, U_{vc} and U_{vv} are coupling constants of the short range potential of vacancies for conduction and valence bands, a is the lattice constant, ω_0 is the frequency of optical phonons, and ρ is the mass density. N_v is the concentration of vacancies calculated from the condition that one vacancy gives two charge carriers, $N_v=n/2$. The parameters used for calculation of the relaxation times in bulk PbTe at T=300 K are taken from Ref. [49]. These parameters are shown in Table 4.1. For calculations at different temperatures we assumed the values of these parameters to be the same as for T=300 K except for E_g and m_t^*, which were linearly interpolated and extrapolated using T=4.6 K and T=300 K values[49], with E_g saturating for T>400 K [47].

4.2 ELECTRON SCATTERING ON BAND-BENDING POTENTIAL OF NANOINCLUSIONS

4.2.1. Band-bending potential

In our model we assume that spherical metallic nanoinclusions with radius R and volume fraction x are randomly distributed in a n-doped PbTe host material. In this section we will calculate the contribution to the relaxation time due to scattering of electrons on the band-bending potential at the metal-semiconductor interface. For a *single* nanoinclusion, the electrostatic potential $V(r)$ can be calculated by solving the Poisson equation

$$\frac{\epsilon_0}{4\pi e^2}\frac{1}{r}\frac{d^2}{dr^2} rV(r) = n[E_F] - n[E_F - V(r)]. \tag{4.15}$$

The right-hand-side of this expression is simply the spatially varying charge (see Eq. 4.2)) calculated by assuming a rigid shift of the electronic bands with the local potential *V_r_*. We solve the Poisson equation with the boundary conditions $V(\infty)=0$ and $V(R)=V_B$. (V_B is the potential at the semiconductor/metal interface. The value of V_B is fixed for a particular metal and depends on the detailed properties of the interface. However, one may consider it to be an optimization optimization parameter provided that the physics of the metal/ semiconductor interface allows tailoring of V_B by choosing the metal.) We used the fourth-order Runge-Kutta and shooting methods in order to solve Eq. 4.15. Figure 4.1b shows an example of the calculated potential $V(r)$.

For small values of V_B or for large r (when the potential is screened and small) the right-hand-side of Eq. 4.15 can be linearized with respect to small V:

$$\frac{d^2}{dr^2} rV(r) = \frac{1}{\lambda^2} rV(r), \tag{4.16}$$

where λ is the screening length. The solution of Eq. 4.16 is

$$V(r) \propto \frac{1}{r} e^{-r/\lambda}. \tag{4.17}$$

For degenerate electrons the expression for _ takes the simple form:

$$\frac{1}{\lambda^2} = \frac{2e^2(2m_d^*)^{3/2}}{\epsilon_0 \pi \hbar^3} \left(E_F + \frac{E_F^2}{E_g} \right)^{1/2} \left(1 + 2\frac{E_F}{E_g} \right). \tag{4.18}$$

Due to the large value of the dielectric constant in PbTe, ε_0=400, the screening length for typical doping concentrations is several times larger than the wavelength of electrons on the Fermi surface. For example, for n=5X10^{19} cm^{-3} one can obtain from Eq. 4.18 λ=11 nm and $k_F\lambda$ =7, where k_F is the wave vector of the electron on the Fermi surface. This value of $k_F\lambda$ slowly varies with doping (for degenerate electrons we can use Eqs. 4.2 and 4.18 to obtain the dependence on doping $k_F\lambda \propto n^{1/6}$). On the other hand, a large value of λ can lead to an overlap of the band bending between nanoparticles, which may change the bulk carrier concentration. We have restricted our calculations to a parameter range (doping and inclusion volume fraction) where such effects are not significant.

4.2.2. Relaxation time for scattering on nanoinclusions

When the electron scattering on nanoinclusions is taken into account, the total relaxation time τ is

$$\tau^{-1} = \tau_{\text{bulk}}^{-1} + \tau_i^{-1}, \tag{4.19}$$

where the relaxation time for bulk PbTe is given by Eq. 4.7 and τ_i is the relaxation time due to scattering by $V(r)$ at randomly distributed metallic inclusions

$$\tau_i^{-1} = n_i \upsilon \sigma_t. \tag{4.20}$$

Here

$$n_i = 3x/(4\pi R^3) \tag{4.21}$$

is the concentration of inclusions, σ_t is the electronic transport scattering cross section, and $v = \partial_p E_p$ is the electronic velocity with p the momentum.

In order to calculate the transport cross section in a system with nonparabolic energy dispersion, we consider an electron with momentum $\mathbf{p}$ and wave function $\psi_{\mathbf{p}}(\mathbf{r}) = u_p(\mathbf{r}) e^{i\mathbf{pr}/\hbar}$ in the periodic field of the unperturbed PbTe crystal of unit volume. Here $u_{\mathbf{p}}(\mathbf{r})$ is the periodic Bloch amplitude. As mentioned earlier, the nonparabolicity of the electron energy dispersion near the conduction band minima is usually described by the Kane model[47]

$$E_p(1 + E_p/E_g) = p^2/2m_{d1}^*. \tag{4.22}$$

The isotropic energy dispersion in a form of Eq. 4.22 with density of state mass m_{d1}^* is usually assumed in the calculation of the relaxation time[47-49]. The transition probability for scattering from state $\psi_{\mathbf{p}i}$ to state $\psi_{\mathbf{p}f}$ per unit time due to a perturbation potential $V(r)$ is given by the standard formula of perturbation theory[50]

$$dw_{fi} = \frac{2\pi}{\hbar} \left| V_{\mathbf{p}_f \mathbf{p}_i} + \int \frac{V_{\mathbf{p}_f \mathbf{p}_1} V_{\mathbf{p}_1 \mathbf{p}_i}}{E_{p_i} - E_{p_1}} d\nu_1 + \ldots \right|^2 \times \delta(E_{p_f} - E_{p_i}) d\nu_f, \tag{4.23}$$

where $d\nu = d^3\mathbf{p}/(2\pi\hbar)^3$. The matrix elements are

$$V_{\mathbf{p}'\mathbf{p}} \equiv \int \psi^*_{\mathbf{p}'}(\mathbf{r}) V(\mathbf{r}) \psi_{\mathbf{p}}(\mathbf{r}) d^3\mathbf{r} \approx \int e^{i(\mathbf{p}-\mathbf{p}')\mathbf{r}/\hbar} V(\mathbf{r}) d^3\mathbf{r}, \tag{4.24}$$

where we used the fact that collisions with a small momentum transfer dominate scattering on the slow-varying bendbending potential, therefore, the Bloch amplitudes entering Eq. 4.24 are rather close to each other, and the overlap factor is about unity $\int u^*_{\mathbf{p}'}(\mathbf{r}) u_{\mathbf{p}}(\mathbf{r}) d^3\mathbf{r} \approx 1$.

Applying Eq. 4.24 to Eq. 4.23, the calculation of dw_{fi} becomes identical to the calculation of the transition probability for scattering of a plane wave $e^{i\mathbf{p}_i\mathbf{r}/\hbar}$ in a model system described by an equation

$$(E_{\hat{p}} + V)\psi = E_p \psi \tag{4.25}$$

with unperturbed Hamiltonian $E_{\hat{p}}, \hat{\mathbf{p}} \equiv -i\hbar\partial_r$ and perturbation potential $V(\mathbf{r})$. Applying the operator $1 + E_{\hat{p}}/E_g$ to Eq. 4.25 one obtains

$$\frac{\hat{p}^2}{2m^*_{d1}}\psi = \left[\frac{p^2}{2m^*_{d1}} + \frac{V^2}{E_g} - V\left(1 + 2\frac{E_p}{E_g}\right)\right]\psi. \tag{4.26}$$

Here we neglect the commutator term $E_g^{-1}[E_{\hat{p}}, V(r)]\psi$

$$E_g^{-1}[E_{\hat{p}}, V(r)] \approx \frac{E_F}{E_g}\frac{1}{(k_F\lambda)^2}V(r) \ll V(r) \tag{4.27}$$

using the fact that $rV(r)$ is a slow varying function and $k_F\lambda >> 1$.

Equation 4.26 has the form of the usual Schrödinger equation that can be used for numerical solution of the scattering problem with a potential

$$U_p(r) = V(r)\left(1 + 2\frac{E_p}{E_g}\right) - \frac{V^2(r)}{E_g}. \tag{4.28}$$

4.2.3. Calculation of transport cross section

The transport cross section for scattering on the spherically symmetric potential is given by[50]

$$\sigma_t = 2\pi \int_0^{\pi} |f(\theta)|^2 (1 - \cos\theta) \sin\theta d\theta, \tag{4.29}$$

where $f(\theta)$ is the scattering amplitude defined from the large -r asymptote of the wave function

$$\psi \approx e^{i\mathbf{pr}/\hbar} + \frac{f(\theta)}{r} e^{ipr/\hbar}. \tag{4.30}$$

The wave function ψ is a solution of the Schrödinger Eq. 4.26 with potential $U_p(r)$ given by Eq. 4.28. It can be expressed as a sum of contributions with different angular momentum l *[50]*

$$\psi = \sum_{l=0}^{\infty} P_l(\cos\theta) R_{kl}(r), \tag{4.31}$$

where P_l are the Legendre polynomials and $R_{kl}(r)$ are solutions of the radial Schrödinger equation $(k = p/\hbar)$:

$$\psi = \sum_{l=0}^{\infty} P_l(\cos\theta) R_{kl}(r), \tag{4.32}$$

The large-r asymptote of $R_{kl}(r)$ has the form

$$R_{kl}(r) \propto \sin(kr - l\pi/2 + \delta_l)/r, \tag{4.33}$$

where δ_l is the phase shift of $R_{kl}(r)$ relative to the potential free solution. The scattering amplitude $f(\theta)$ can be expressed in terms of the phase shifts as [50]

$$f(\theta) = \frac{1}{2ik}\sum_{l=0}^{\infty}(2l+1)P_l(\cos\theta)(e^{2i\delta_l}-1). \tag{4.34}$$

The calculation of the transport cross section (Eq. 4.29) with scattering amplitude (Eq. 4.34) can be performed in the same way[50] as the usual cross section (without the $(1-\cos\theta)$ factor in Eq. 4.29. In the integrals that appear in the evaluation of the transport cross section (Eq 4.29) , only terms with $l'=l$, $l\pm1$ give nonvanishing contributions [50]. After integration over θ, Eq. 4.29 can be expressed in terms of the δ_l as:

$$\sigma_t = \frac{4\pi}{k^2}\sum_{l=1}^{\infty} l\,\sin^2(\delta_l - \delta_{l-1}). \tag{4.35}$$

We used the following numerical procedure to solve the Schrödinger equation (Eqn 4.32) and calculate the phase shifts. The spherical Bessel function $j_l(kr)$ is a regular solution of Eq. 4.32 for $r<R$, in the region where $U_p(r)=0$. We used the fourth-order Runge-Kutta method to solve Eq.4.32 for $r>R$ with boundary conditions such that the solution $R_l(kr)$ and its derivative match the spherical Bessel function at $r=R$. At some large $r=r_{\max}$ we assume that the potential U_p vanishes and match the solution $R_l(kr)$ and its derivative $R_l'(kr)$ to a linear combination of the spherical Bessel function $j_l(kr)$ and spherical Neumann function $y_l(kr)$ (which is another solution of Eq. 4.32 for $U_p(r)=0$):

$$R_l(kr)|_{r=r_{\max}} \rightarrow \alpha j_l(kr) + \beta y_l(kr), \tag{4.36}$$

with $\alpha = (R_l y_l' - R_l' y_l') / (j_l' y_l' - j_l' y_l)$ and $\beta = -(R_l j_l' - R_l' j_l) / (j_l y_l' - j_l' y_l)$. Finally the phase shift δ_l is given by

$$\delta_l = -\arctan(\beta/\alpha). \tag{4.36}$$

In conjunction with Eqs. 4.20 and 4.35 this provides expressions to numerically calculate τ_i for a given $V(r)$. An example of the numerically calculated τ_i is given in Fig. 4.1c for scattering by $V(r)$ of Fig. 4.1b, with an inclusion volume fraction x=5%. A simple fit gives the dependence $\tau_i(E)\sim E^{1.39}$ as shown by the dashed line in Fig. 4.1c. This energy dependence of $\tau_i(E)$ is much stronger than that of τ_{bulk} and leads to enhancement of the Seebeck coefficient.

To obtain an analytical description of τ_i(E), we also calculated τ_i in the Born approximation by using Fermi's golden rule [first term in r.h.s. of Eq. 4.23]

$$\frac{1}{\tau_i^{\text{Born}}} = \frac{p^2}{2\pi\hbar^4}\frac{dp}{dE}\int_0^{\pi} |V_{\mathbf{p}'\mathbf{p}}|^2(1-\cos\theta)\sin\theta d\theta. \tag{4.38}$$

Here θ is the angle between initial and final momenta **p** and **p**'. The expression for τ_i^{Born} can be simplified by taking the angle integration in Eq. 4.38 for $V_{\mathbf{p}'\mathbf{p}}$ and making the substitutions of integration variables t=2kR sin(θ/2) and y=r /R. Finally one obtains

$$\tau_i^{\text{Born}}(E) = E^{3/2}\frac{(1+E/E_g)^{3/2}}{1+2E/E_g}\frac{R}{x}\frac{4\sqrt{2m_{d1}^*}}{3\alpha(E,R)}, \tag{4.39}$$

where

$$\alpha(E,R) = \int_0^{2kR}\left|\int_1^{\infty}\sin(yt)V(yR)ydy\right|^2 tdt. \tag{4.40}$$

Numerical tests show that for $|V_B|$~<0.1 eV, the Born approximation is valid, τ_i(E)~ $\tau_i^{\text{Born}}(E)$., while for $|V_B|$>0.1 eV, $\tau_i^{\text{Born}}(E)$ begins to deviate from τ_i(E) calculated from the exact solution of Schrödinger's equation (4.32). Nevertheless, Eq. 4.39 allows us to analyze the energy dependence of the relaxation time that is difficult to do by using the exact formulas 4.20 and 4.35. For energies E~>0.1 eV, the integral over variable t in 4.40 weakly depends on the upper limit of the integration, and the function α(E,R) varies slowly with both E and R. Thus, we have $\tau_i^{\text{Born}}(E)\sim E^{3/2}$, in good agreement with the full numerical calculations, which yielded a dependence $E^{1.39}$. Comparing the result $\tau_i^{\text{Born}}(E)\sim E^{3/2}$ with expression 4.20 (and using $v(E)\sim E^{1/2}$), we find that the electronic scattering cross section of the bandbending potential depends on energy as E^{-2}; this strong energy dependence is responsible for the superlinear energy dependence of τ_i(E).

4.3. RESULTS AND DISCUSSION

4.3.1. Enhancement of the Seebeck coefficient and power factor

The calculation of the total relaxation time allows us to obtain S, σ, and κ_e using expressions 4.3-4.5. We first consider a specific case by adopting a simple model for the interface potential V_B=Φ_m−χ+E_F with Φ_m the metal work function and χ the electron affinity, and choose Φ_m−χ=−0.35 eV corresponding to Pb nanoinclusions (work function Φ_m =4.25 eV (Ref. [51])) and an electron affinity for PbTe, χ_{PbTe}=4.6 eV [52]. Figure 4.2 shows the calculated room temperature Seebeck coefficient as a function of the

doping n and fixed nanoinclusion volume fraction x=5%. We note the excellent agreement between the experimentally measured S (filled circles) [53, 54] and that calculated numerically (solid line) for bulk PbTe. In addition, one can see that for any nanoinclusion radius, the Seebeck coefficient is always increased compared to that of the inclusion-free system. In fact, for the smallest nanoinclusion radius considered here (1.5 nm), the enhancement in S is over 100% at high doping.

It is interesting to consider the impact of V_B on the calculated Seebeck coefficient. Figure 4.3a shows S as a function of V_B. It is clearly seen from this figure that the presence of an extended electrostatic potential leads to an increase in S regardless of the sign of V_B. (VB=0 is equivalent to bulk PbTe with nanoinclusions. Negative values correspond to the situation of Fig. 1, and positive values represent a Schottky barrier.) This general behavior can be understood (at least for small $|V_B|$) from the Born approximation, which predicts that the inverse scattering time is proportional to the square of the perturbation potential. With increase of $|V_B|$ the contribution to the total inverse relaxation time from inclusion scattering increases, leading to an increase of S because the energy dependence of τ changes from that of τ_{bulk} to the more strongly energy dependent τ_i. For large values of $|V_B|$ the contribution of island scattering becomes dominant, and S saturates as seen in Fig. 4.3a. Figure 4.3a also shows the calculated values of σ as a function of the interface potential V_B. The conductivity decreases as $|V_B|$ is increased, with a fairly symmetric behavior for $\pm VB$. Combining the results for s and S, we obtain the power factor S^2s as depicted in Fig. 4.3b. There, one can see that the power factor is increased compared to that at V_B =0, in a range of interface potentials −0.15 eV<V_B <0.15 eV. The power factor has two maxima at some optimal values of VB because the Seebeck coefficient saturates for large $|V_B|$, while the electrical conductivity σ continues to decrease with increase of $|V_B|$.

For the optimal interface potential V_B~±0.07 eV, we find that the power factor is increased by ~35%. Importantly, the power factor does not decrease substantially over a wide range of values of the interface potential. Thus, it is possible to take full advantage of the reduction in thermal conductivity due to phonon scattering at the nanoinclusions, as we will discuss later.

Instead of optimizing the value of the interface potential V_B to achieve the maximum power factor as shown in Fig. 4.3b, we can keep V_B fixed (by choosing a specific metal for the inclusions) and optimize other parameters, for example the inclusion volume fraction or radius. To analyze the dependence of the transport coefficients on these parameters, we can use Eq. 4.39. As we noted above, the function $\alpha(E,R)$ in Eq. 4.40 varies slowly with both E and R, so the inverse relaxation time due to electron scattering by inclusions can be approximated as $\tau_i^{-1}(E)$~$CE^{-3/2}$, where the constant C depends on V_B, x, and R mostly through the combination (at least for small V_B)

$$C \propto V_B^2 x/R. \tag{4.41}$$

In turn, the transport coefficients (S, σ, and κ_e) depend only on this ratio of

parameters. This means that if any two parameters out of these three are fixed, one can always adjust the third parameter (for example, the one that can be most easily tuned in the experiment) to maximize the power factor.

Before closing this section, we remark that we have searched for resonant tunneling states in the positive V_B regime as a way to enhance S. However, we have not found any significant increase in S beyond that already discussed. The reason is that, because the potential contains contributions from several Legendre polynomials l, the appearance of a resonant state for one value of l is washed out by the nonresonant conditions in the other channels.

4.3.2. Enhancement of the zT factor

While S and σ are quantities of fundamental interest, for applications it is usually $zT=S^2\sigma T/\kappa$ that is most important. The electronic relaxation time calculated above leads directly to the electronic thermal conductivity κ_e. Since the total thermal conductivity is the sum of electronic and phonon contributions, $\kappa=\kappa_e+\kappa_{ph}$, to obtain zT we also need to calculate κ_{ph}. For this purpose, we adopt a previous method[55, 56] that considered the scattering of phonons on nanoinclusions, with the scattering mechanism for short wavelength phonons being the different sound velocities in the host and nanoinclusions. This approach has been shown to give excellent agreement with experiments on nanoscale ErAs inclusions in InGaAs [55]. For T~>T_D (T_D=130 K is the Debye temperature of PbTe) κ_{ph} can be written as[47]

$$\kappa_{ph} \approx \frac{k_B}{2\pi^2 v_s \hbar^3}\int_0^{k_B T_D} \tau_{ph}(\hbar\omega)^2 d(\hbar\omega), \tag{4.42}$$

where v_s is the speed of sound in PbTe, and $\hbar\omega$ is the phonon energy. The phonon relaxation time τ_{ph} is given by

$$\tau_{ph}^{-1} = \tau_U^{-1} + \tau_D^{-1}, \tag{4.43}$$

where $\tau_U^{-1}=cT\omega^2$ is the contribution of umklapp scattering[47] and τ_D is due to scattering by nanoinclusions. The constant c was determined from Eq. 4.42 using the experimental value κ_{ph}^{bulk}=2.0 W/mK for PbTe at T=300 K. For τ_D we used the expression derived in Refs. [55] and [56]. In the near-geometrical scattering regime (qR~>1) τ_D reads

$$\tau_D^{-1} = n_i v_s (2\pi R^2)[1 - \sin(2\xi)/\xi + \sin^2(\xi)/\xi^2], \tag{4.44}$$

where $\xi=qR(v_s/v_s'-1)$, q is the phonon wave vector, and v_s' is the speed of sound inside

the inclusion. Numerical tests show that when the difference in the sound velocities is larger than 20% the integrated quantity κ_{ph} weakly depends on this difference and τ_D can be approximated by its geometrical limit value

$$\tau_D^{-1} = n_i v_s (2\pi R^2) = \frac{3}{2}\frac{x}{R} v_s . \tag{4.45}$$

Note that this phonon scattering regime is opposite to that on point defects where qR<<1.

Figure 4.4 shows zT and its components calculated for x =5%, R=1.5 nm, and a doping n=2.5X10^{19} cm^{-3}, as a function of temperature. We discuss this doping first because experimental values of zT and all of its components are readily available for inclusion-free PbTe, and can be compared with our calculations; indeed, the calculated values for zT, S, σ, and κ (solid lines in Fig. 4.4a-4.4d) are in good agreement with experiment[54] (filled squares) for T<~700 K. (The deviations for T~>700 K originate in our neglect of the hole contribution to the charge and heat transport). In the presence of nanoinclusions, the individual components of zT deviate from their bulk PbTe values at all temperatures shown. For T~>400 K the increase of the Seebeck coefficient is compensated by decrease of the conductivity, and the optimized power factor is close to that of bulk PbTe (see inset in Fig. 4.4c). At such temperatures the small increase of the zT factor due to "electron-only" scattering by nanoinclusions (open circles in Fig. 4.4a) is a result of the decrease in κ_e (open circles in Fig. 4.4d). Comparing the zT shown by filled and open circles in Fig. 4.4a, one can conclude that at a doping n=2.5X10^{19} cm^{-3} the enhancement of the optimized zT is primarily due to decrease of κ_{ph}, at least for T~>400 K.

To get a more comprehensive understanding of the role of nanoinclusions in enhancing the thermoelectric properties, we show in Fig. 4.5 the room-temperature zT factor as a function of the interface potential for two values of the doping. In addition, we plot zT calculated using the bulk value of the phonon thermal conductivity κ_{ph}^{bulk} (dotted lines). We first consider the situation of high doping, as depicted in Fig. 4.5a. In the absence of a spatially-varying potential (V_B=0) and without phonon scattering on nanoinclusions, zT is given by the filled circle. Turning on the phonon scattering gives a modest 25% increase in zT (the star in the figure). Similarly, one can consider the increase in zT without phonon scattering on the nanoinclusions (dotted line); in this case, a large increase in zT of up to 224% is obtained. Thus at this doping, electron scattering can give a much larger increase in zT. However, the true advantage of nanoinclusions is realized when *both* electron and phonon scattering are included, and the zT factor can be increased by as much as 430%. This increase is much larger than simply the sum of the individual electronic and phonon contributions.

The origin of this behavior lies in the nonadditive effects of electronic and phonon thermal conductivities, since zT depends inversely on their sum. For the large doping situation of Fig. 4.5a we have κ_e^{bulk}=4.2W/mK, κ_{ph}^{bulk} =2.0 W/mK, and therefore $\kappa_{ph}^{bulk}<\kappa_e^{bulk}$. In this case, reducing κ_{ph} by itself does not lead to an appreciable gain in

zT. However, when κ_e is also reduced because of scattering and becomes comparable to κ_{ph}, then both work in concert and lead to a large increase in zT. Thus, one can imagine that electron scattering on the electrostatic potential serves as an amplification mechanism to enhance the impact of the reduction in phonon thermal conductivity. This mechanism works here because at high doping (i) $\kappa_{ph}^{bulk}<\kappa_e^{bulk}$ and (ii) the power factor is maintained or even enhanced in a wide range of interface potentials.

The situation is quite different in the case of low doping, where $\kappa_{ph}^{bulk}>>\kappa_e^{bulk}$, as illustrated in Fig. 4.5b. In this case, the electronic thermal conductivity is already quite low, κ_e^{bulk} =0.6 W/mK < κ_{ph}^{bulk} =2.0 W/mK, and the main impact of nanoinclusions is to decrease the phonon thermal conductivity. The maximum increase in zT is 107%, with 94% coming from phonons alone. In fact, for this low doping, the power factor is always reduced compared to the inclusion-free system——a signature of this effect is the reduction of zT below that of the inclusion-free system for larger values of V_B.

Figure 4.6 shows the calculated zT as a function of temperature for low (n=5X10^{18} cm^{-3}) and high (n=5 X10^{19} cm^{-3}) doping levels. Included in the figure are the zT factor calculated with both electron and phonon scattering on nanoinclusions (filled circles), that calculated with electron- only scattering on nanoinclusions and with bulk PbTe values of κ_{ph} (open circles), and the zT calculated for inclusion-free bulk PbTe (solid line). The corresponding values of V_B that maximize zT are shown in the insets by filled circles. The inset in Fig. 4.6a shows that at n=5X10^{18} cm^{-3}, the optimal V_B is very small $|V_B|$= 0.03 eV and even vanishes for T > 600 K. Thus, the electron contribution to enhancement of optimized ZT is negligible (solid line and line with open circles almost coincide in Fig. 4.6a) and, the enhancement of the optimized zT is dominated by the reduction in κ_{ph} due to phonon scattering on the inclusions. This can be explained by the fact that for bulk PbTe, the Seebeck coefficient increases with decrease of the doping concentration n, and the *relative* enhancement of the Seebeck coefficient from its bulk value due to electron scattering on inclusion is smaller at low doping compared to high doping (see Fig. 4.2). As a consequence the reduction of σ at low doping overweights the increase of S^2, and the power factor is reduced compared to the inclusion-free system, leading to small or vanishing optimal V_B. From a practical point of view this result means that in order to enhance the zT factor at low-doping levels one needs to find a metal that gives little or no interfacial potential.

For larger doping the electron contribution to enhancement of zT becomes important, and the optimized V_B increases. It is seen in Fig. 4.6b that for n=5X10^{19} cm^{-3}, the electron-only contribution to enhancement of the optimized zT makes up over 50% of the enhancement at T<~600 K, and the optimized V_B is as large as 0.2 eV. Moreover, at large doping, $\kappa_e^{bulk}>\kappa_{ph}^{bulk}$, and the reduction of κ_e due to scattering on inclusions amplifies the effect of the reduced κ_{ph}. The upper inset in Fig. 4.6b shows that the power factor $S^2\sigma$ is enhanced only for T<600 K. The reduction of the power factor relative to the inclusion-free system at T>600 K is due to the fact that at high temperature, the Seebeck coefficient of bulk PbTe is already large (see Fig. 4.4b); the *relative* increase in S induced by electron scattering on inclusions becomes smaller at increased temperature, so the reduction of σ overweights the increase of S^2. Nevertheless, the electron-only contribution results in enhancement of zT (open circles in Fig. 4.6b) even at higher temperatures due to reduction of κ_e.

Figure 4.6b shows by open squares the zT factor for PbTe with Pb inclusions (assuming $V_B^{Pb}-E_F=-0.35$ eV) for parameters $n=5X10^{19}$ cm^{-3}, R=1.5 nm, and x=5%. For this set of parameters the interface potential V_B^{Pb} is close to the optimal one (see inset in Fig. 4.6b) in a wide range of temperatures, so the zT factor for the system with Pb inclusions is very close to the optimal zT. The enhancement of zT due to Pb inclusions is on the order of 400% at room temperature and 50% at T=900 K, where it reaches a value as high as 1.5.

4.4 CONCLUSION

In conclusion, we developed a theory that allows the calculation of the zT factor and its components for a system of a semiconductor host material with spherical metallic nanoinclusions. The enhancement of the Seebeck coefficient can be explained by a strong energy dependence of electron scattering on the band bending at the interface between metallic inclusions and the semiconductor host. The electronic contribution to enhancement of zT is important for high doping, while at low doping the enhancement of zT is dominated by the reduction in the phonon thermal conductivity. The theory can be used to choose the optimal parameters for the metal nanoinclusions (interface potential, inclusion volume fraction or radius) in order to maximize zT.

Parameter	Value	Parameter	Value
E_g	0.315 eV	$\hbar\omega_0$	0.0136 eV
m_t^*/m_0	0.0453	a	6.461 Å
m_l^*/m_0	0.24	ρ	8.24 g/cm
ϵ_0	400	E_{ac}	15 eV
ϵ_∞	32.6	E_{oc}	26 eV
C_l	7.1×10^{10} N/m	$K_{a,o}$	1.5
U_{vc}	3×10^{-34} erg cm^3	K_v	1.5

Table 4.1 Parameters used to calculate the relaxation times for bulk PbTe at T=300 K [49]. m_0 is the free electron mass.

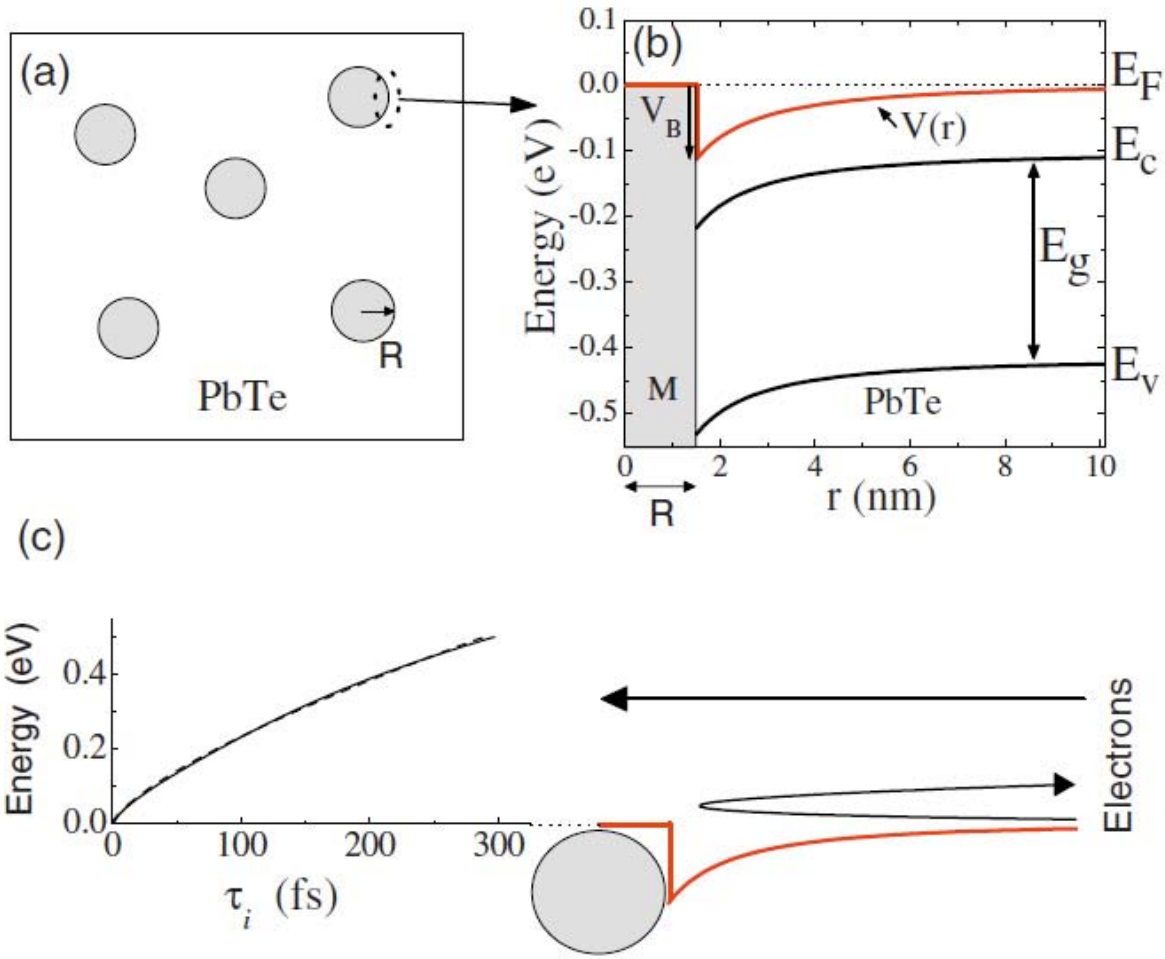

Figure 4.1 (a) Schematic of the semiconductor host with metallic nanoinclusions. Panel (b) shows an example of the calculated potential $V(r)$ and the energy diagram for PbTe at T =300 K, n=2.5X10^{19} cm^{-3}, V_B=−0.11 eV, and R=1.5 nm. Panel (c) illustrates the concept of energy filtering: low energy electrons scatter strongly with the potential, but high energy electrons are unaffected. The calculated electronic relaxation time for the potential of panel (b) is also shown.

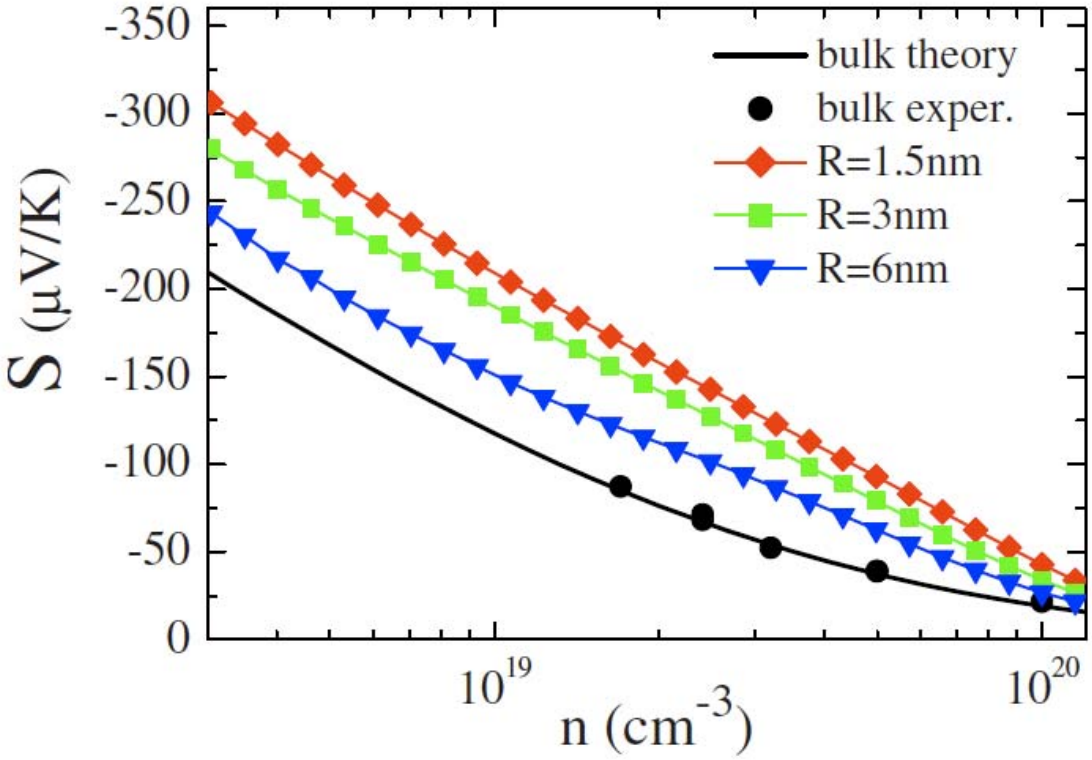

Figure 4.2 Calculated Seebeck coefficient for PbTe with metallic nanoinclusions as a function of the doping for severaldifferent values of the nanoinclusion radius.

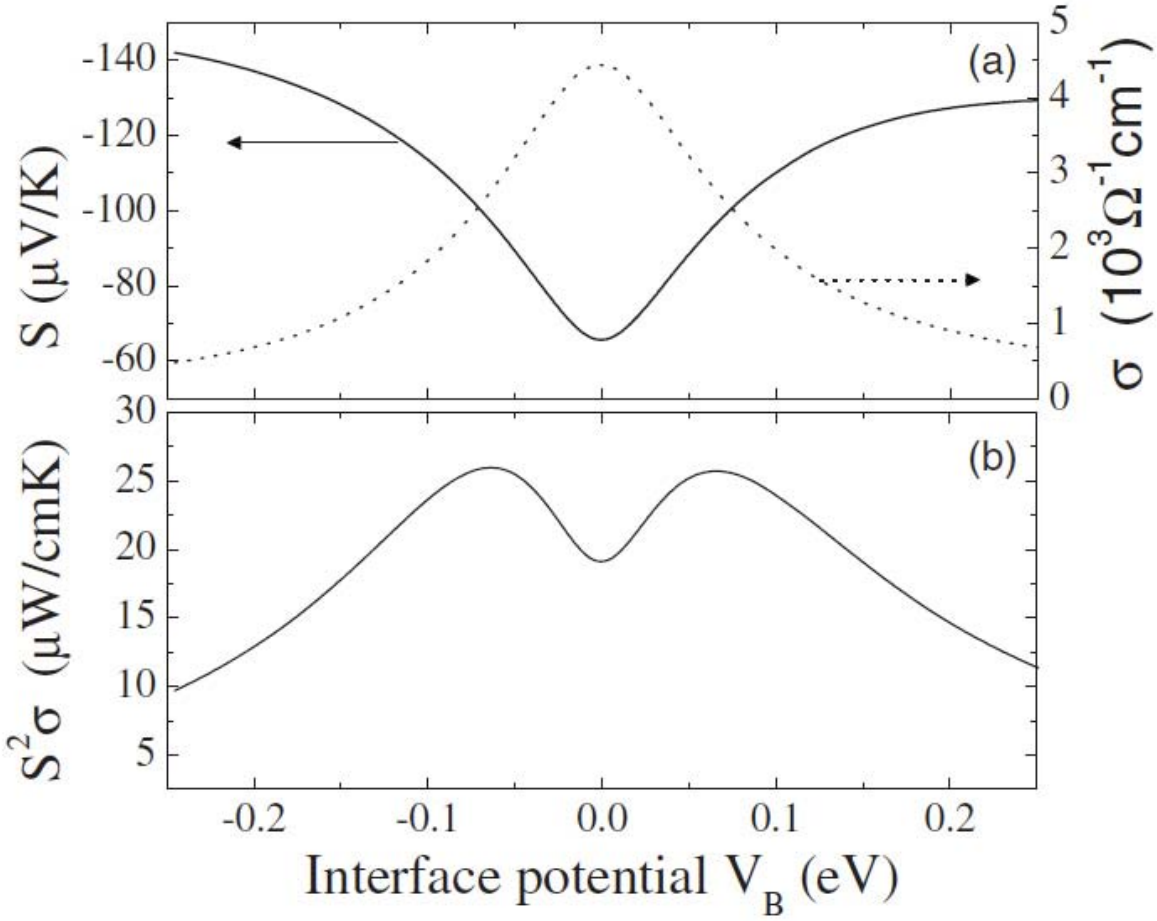

Figure 4.3 Panel (a) shows the calculated Seebeck coefficient and conductivity for PbTe as a function of the interface potential V_B. Panel (b) shows the resulting power factor. Parameters are R=1.5 nm, T=300 K, x=5%, and n=2.5X10^{19} cm^{-3}.

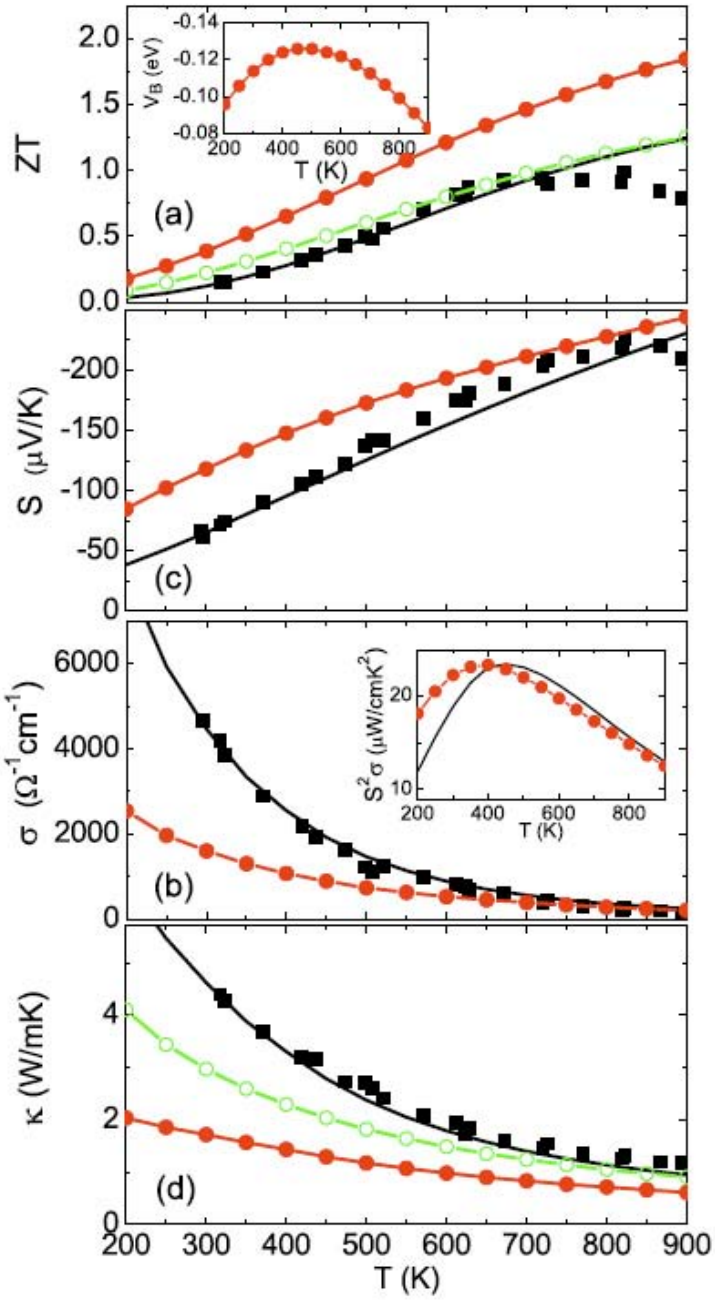

Figure 4.4 Thermoelectric coefficients as a function of temperature calculated for n=2.5X10^{19} cm−3, x=5%, and R=1.5 nm. (a) The optimized zT factor, with the optimal values of V_B, is shown in the inset. (b) The Seebeck coefficient. (c) The electrical conductivity. Inset shows optimized (filled circles) and bulk PbTe (solid line) power factor $S^2\sigma$. (d) The thermal conductivity. In all panels, solid circles include electron and phonon scattering on the inclusions; open circles include electron scattering onthe inclusions but with bulk PbTe values of κ_{ph}; solid lines and filled squares are the calculated and measured Ref. [54] values for bulk PbTe.

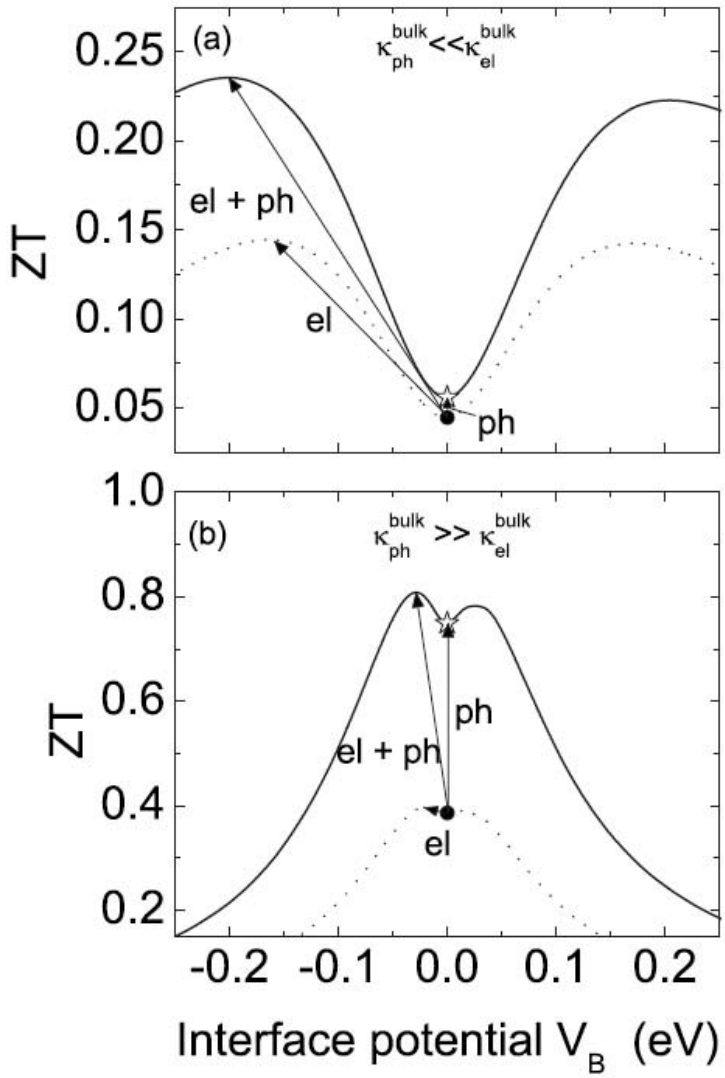

Figure 4.5 Calculated ZT factor for PbTe illustrating the relative effects of electronic and phonon scattering on nanoinclusions. In both panels *R*=1.5 nm, *x*=5%, and *T*=300 K. (a) High doping n=5X10^{19} cm^{-3}. (b) Low doping n=5X10^{18} cm^{-3}. Dotted lines are calculated using the bulk phonon thermal conductivity. Filled circles correspond to the bulk PbTe system. Stars include only the phonon scattering on nanoinclusions.

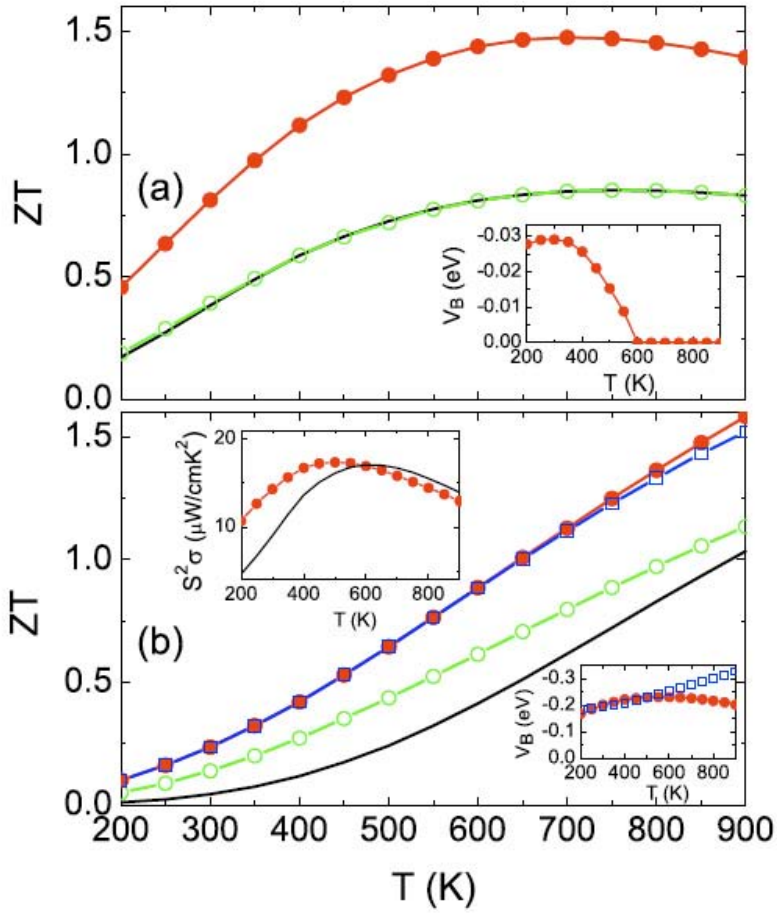

Figure 4.6 Temperature dependence of the optimized *ZT* factor for PbTe. (a) low doping n=5X10^{18} cm^{-3} and (b) high doping n=5X10^{19} cm^{-3}. In both panels filled circles denote the optimized *zT* calculated with both electron and phonon scattering on nanoinclusions, open circles denote *zT* calculated with electron scattering on nanoinclusions and with bulk PbTe values of κ_{ph}, and the solid line is for bulk PbTe. The inset in (a) shows the values of V_B that maximize *zT*. In (b) the bottom inset shows the optimal values of V_B that maximize *zT* (filled circles) and V_B^{Pb} for Pb nanoinclusions. The top inset shows the calculated power factor.

References

1. Rowe, D.M., *Thermoelectrics Handbook: Macro to Nano*. 2006: CRC Press, Taylor and Francis.
2. Hsu, K.F., et al., *Cubic $AgPb_mSbTe_{2+m}$ Bulk Thermoelectric Materials with High Figure of Merit.* Science, 2004. **303**: p. 818-821.
3. Heremans, J.P., C.M. Thrush, and D.T. Morelli, *Thermopower Enhancement in PbTe with Pb Precipitates.* Journal of Applied Physics, 2005. **98**: p. 063703.
4. Snyder, G.J. and E.S. Toberer, *Complex Thermoelectric Materials.* Nature Materials, 2008. **7**: p. 105-114.
5. Dughaish, Z.H., *Lead Telluride as a Thermoelectric Material for Thermoelectric Power Generation.* Physica B, 2002. **322**: p. 205-223.
6. Rosi, F.D., E.F. Hockings, and N.E. Lindenblad, *Semiconducting Materials for Thermoelectric Power Generation.* RCA Review, 1961. **22**(1): p. 82-121.
7. Nolas, G.S., J. Sharp, and H.J. Goldsmid, *Thermoelectrics: Basic Principles and New Materials Developments*. 2001, Berlin, Heidelberg: Springer-Verlag.
8. Cook, N.J., et al., *Minerals of the System Bi-Te-Se-S Related to the Tetradymite Archetype: Review of Classification and Composiitional Variation.* The Canadian Mineralogist, 2007. **45**(4): p. 665-708.
9. Medlin, D.L. and G.J. Snyder, *Interfaces in Bulk Thermoelectric Materials.* Current Opinion in Colloid and Interface Science, 2009. **14**: p. 226-235.
10. Jovovic, V. and J.P. Heremans, *Doping Effects on the Thermoelectric Properties of $AgSbTe_2$.* Journal of Electronic Materials, 2009: p. DOI:10.1007/s11664-009-0669-7.
11. Skrabek, E.A. and D.S. Trimmer, *Properties of the General TAGS System*, in *CRC Handbook of Thermoelectrics*, D.M. Rowe, Editor. 1995, CRC Press Inc.: Boca Raton. p. 267-275.
12. Sugar, J.D. and D.L. Medlin, *Precipitation of Ag_2Te in the Thermoelectric Material $AgSbTe_2$.* Journal of Alloys and Compounds, 2009. **478**: p. 75-82.
13. Maier, R.G., *Zur Kenntnis des Systems PbTe-$AgSbTe_2$.* Zeitschrift für Metallkunde, 1963. **54**(5): p. 311-312.
14. Geller, S., *Ternary Semiconducting Compounds with Sodium Chloride-Like Structure: $AgSbSe_2$, $AgSbTe_2$, $AgBiS_2$, $AgBiSe_2$.* Acta Crystallographica, 1959. **12**: p. 46.
15. Quarez, E., et al., *Nanostructuring, Compositional Fluctuations, and Atomic Ordering in the Thermoelectric Materials $AgPb_mSbTe_{2+m}$. The Myth of Solid Solutions.* J. American Chemical Society, 2005. **127**: p. 9177-9190.
16. Armstrong, R.W., J.W. Faust, and W.A. Tiller, *A Structural Study of the Compound $AgSbTe_2$.* Journal of Applied Physics, 1960. **31**(11): p. 1954-1959.
17. McHugh, J.P., et al., *Phase Diagram for the Pseudobinary System Ag2Te-Sb2Te3.* Journal of Applied Physics, 1961. **32**(9): p. 1785.

18. Offergeld, G., et al., *Sur la Decomposition Eutectoide de $AgSbTe_2$.* Comptes Rendus Hebdomadaires des Seances de L'Academie des Sciences, 1961. **252**(24): p. 3788.
19. Marin, R.M., G. Brun, and J.-C. Tedenac, *Phase Equilibria in the Sb_2Te_3-Ag_2Te system.* Journal of Materials Science, 1985. **20**: p. 730-735.
20. Matsushita, H., E. Hagiwara, and A. Katsui, *Phase diagram and the Thermoelectric Properties of $Ag_{3-x}Sb_{1+x}Te_3$ System.* Journal of Materials Science, 2004. **39**: p. 6299-6301.
21. Manolikas, C., *A Study by Means of Electron Microscopy and Electron Diffraction of the Phase Transformation and the Domain Structure in Ag_2Te.* Journal of Solid State Chemistry, 1987. **66**: p. 1-6.
22. Schneider, J. and H. Schulz, *X-ray powder diffraction of Ag_2Te at temperatures up to 1123 K.* Zeitschrift für Kristallographie, 1993. **203**: p. 1-15.
23. Ayral-Marin, R.M., et al., *Contribution to the study of $AgSbTe_2$.* European Journal of Solid State and Inorganic Chemistry, 1990. **27**(5): p. 747-757.
24. Wolfe, R., J.H. Wernick, and S.E. Haszko, *Anomalous Hall Effect in AgSbTe2.* Journal of Applied Physics, 1960. **31**(11): p. 1959-1964.
25. Burmeister, R.A. and D.A. Stevenson, *Preparation and Electric Properties of Silver Antimony Telluride.* Transactions of the Metallurgical Society of AIME, 1964. **230**: p. 329-332.
26. Stegherr, A., F. Wald, and P. Eckerlin, Z. Naturforsch. Pt. A, 1961. **16**: p. 130.
27. Ikeda, T., et al., *Self-Assembled Nanometer Lamellae of Thermoelectric PbTe and Sb_2Te_3 with Epitaxy-Like Interfaces.* Chem. Mater., 2007. **19**: p. 763-767.
28. Ikeda, T., et al., *Solidification Processing of Alloys in the Pseudo-Binary PbTe-Sb_2Te_3 System.* Acta Materialia, 2007. **55**: p. 1227-1239.
29. Ikeda, T., V. Ravi, and G.J. Snyder, *Formation of Sb_2Te_3 Widmanstätten Precipitates in Thermoelectric PbTe.* Acta Materialia, 2009. **57**: p. 666-672.
30. Ikeda, T., et al., *In situ Observation of Eutectoid Reaction Forming a PbTe-Sb_2Te_3 Thermoelectric Nanocomposite by Synchrotron X-ray Diffraction.* Scripta Materialia, 2009. **60**: p. 321-324.
31. Hirth, J.P., *Dislocations, Steps and Disconnections at Interfaces.* J. Phys. Chem. Solids, 1994. **55**(10): p. 985-989.
32. Pond, R.C. and J.P. Hirth, *Defects at Surfaces and Interfaces.* Solid State Physics, 1994. **47**: p. 287-365.
33. Hirth, J.P. and R.C. Pond, *Steps, Dislocations and Disconnections as Interface Defects Relating to Structure and Phase Transformations.* Acta Materialia, 1996. **44**(12): p. 4749-4763.
34. Frangis, N., et al., *Continuous Series of One-Dimensional Structures in Compounds Based on M_2X_3 (M=Sb,Bi; X=Se,Te).* Journal of Solid State Chemistry, 1990. **84**: p. 314-334.
35. Anderson, T.L. and H.B. Krause, *Refinement of the Sb_2Te_3 and Sb_2Te_2Se Structures and Their Relationship to Nonstoichiometric $Sb_2Te_{3-y}Se$ Compounds.* Acta Cryst., 1974. **B30**: p. 1307-1310.
36. Landauer, R., ed. *Electrical Transport and Optical Properties of Inhomogeneous Media*. ed. J.C. Garland and D.B. Tanner. Vol. 2. 1978, AIP: New York.

37. Bergman, D.J. and O. Levy, *Thermoelectric Properties of a Composite Medium.* Journal of Applied Physics, 1991. **70**(1): p. 6821-6833.
38. Morelli, D.T., V. Jovovic, and J.P. Heremans, *Intrinsically Minimal Thermal Conductivity in Cubic I-V-VI$_2$ Semiconductors.* Physical Review Letters, 2008. **101**: p. 035901.
39. Aliev, S.A. and S.S. Ragimov, *Thermoelectric Properties of Samples of the Ag-Sb-Te System.* Inorganic Materials, 1992: p. 239-243.
40. McLachlan, D.S., M. Blaszkiewicz, and R.E. Newnham, *Electrical Resistivity of Composites.* Journal of the American Ceramic Society, 1990. **73**(8): p. 2187-2203.
41. Bergman, D.J. and O. Levy, *Scaling Behavior of the Thermopower in a 2-Component Composite Near the Percolation Threshold.* Journal of Physics A-Mathematical and General, 1992. **25**(7): p. 1875-1884.
42. Gelbstein, Y., *Thermoelectric Power and Structural Properties in Two-Phase Sn/SnTe Alloys.* Journal of Applied Physics, 2009. **105**: p. 023713.
43. Lostak, P., et al., *Transport Coefficients and Defect Structure of Sb2-xAgxTe3 Single Crystals.* Journal of Physics and Chemistry of Solids, 2006. **67**(7): p. 1457-1463.
44. Scher, H. and R. Zallen, *Critical Density in Percolation Processes.* Journal of Chemical Physics, 1970: p. 3759.
45. Porter, D.A., K.E. Easterling, and M. Sherif, *Phase Transformations in Metals and Alloys, 3rd. Edition*. 2009: CRC.
46. Faleev, S.V. and F. Léonard, *Theory of Enhancement of Thermoelectric Properties of Materials with Nanoinclusions.* Physical Review B, 2008. **77**: p. 214304.
47. Ravich, Y.I., B.A. Efimova, and I.A. Smirnov, *Semiconducting Lead Chalcogenides*. 1970, New York: Plenum.
48. Ravich, Y.I., B.A. Efimova, and V.I. Tamarchenko, Phys. stat. sol. B, 1971. **43**: p. 11.
49. Zayachuk, D.M., Semiconductors, 1997. **31**: p. 173.
50. Landau, L.D. and E.M. Lifshitz, *Quantum Mechanics Nonrelativistic Theory, Course of Theoretical Physics, 3rd Edition.* Vol. 3. 1976, Moscow: Nauka.
51. Michaelson, H.B., Journal of Applied Physics, 1977. **48**: p. 4729.
52. Spicer, W.E. and G.T. Lapeyre, Physical Review A, 1965. **565**.
53. Ravich, Y.I., B.A. Efimova, and V.I. Tamarchenko, Phys. stat. sol. B, 1971. **43**: p. 453.
54. Efimova, B.A., et al., Sov. Phys. Semicond, 1971. **4**: p. 1653.
55. Kim, W., et al., *Thermal Conductivity Reduction and Thermoelectric Figure of Merit Increase by Embedding Nanoparticles in Crystalline Semiconductors.* Physical Review Letters, 2006. **96**: p. 045901.
56. Kim, W. and A. Majumdar, *Phonon Scattering Cross Section of Polydispersed Spherical Nanoparticles.* Journal of Applied Physics, 2006. **99**: p. 084306.

Distribution

1	MS9161	Douglas Medlin	8656
1	MS9161	Sarah Allendorf	8656
2	MS9018	Central Technical Files	8944
2	MS0899	Technical Library	4536
1	MS0123	D. Chavez, LDRD Office	1011